

1 Two decades of pH_T measurements along the GO-SHIP A25 section 2 in the North Atlantic

3 Fiz F. Pérez¹, Marta López-Mozos^{1,2*}, Marcos Fontela¹, Maribel I. García-Ibáñez³, Noelia Fajar⁴, Xosé
4 Antonio Padín¹, Mónica Castaño-Carrera¹, Mercedes de la Paz¹, Lidia I. Carracedo⁵, Marta Álvarez⁶,
5 Herlé Mercier⁵, Pascale Lherminier⁵, Antón Velo^{1*}

6 ¹Instituto de Investigaciones Marinas (IIM), CSIC, Vigo, 36208, Spain

7 ²Facultad de Ciencias del Mar, Universidade de Vigo, Spain

8 ³Centro Oceanográfico de Illes Balears (COB-IEO), CSIC, Palma, Spain

9 ⁴Centro Oceanográfico de Vigo (COV-IEO), CSIC, Vigo, Spain

10 ⁵University of Brest, CNRS, Ifremer, IRD, Laboratoire d'Océanographie Physique et Spatiale (LOPS), IUEM, Plouzané,
11 29280, France

12 ⁶Centro Oceanográfico de A Coruña (COAC-IEO), CSIC, A Coruña, Spain

13 *Correspondence to: Marta López-Mozos (mlopezm@iim.csic.es) and Antón Velo (avelo@iim.csic.es)

14 Abstract

15 The North Atlantic (NA) GO-SHIP (Global Ship-based Hydrographic Investigation Program) A25 OVIDE-
16 BOCATS (Observatoire de la variabilité interannuelle à décennale en Atlantique Nord - Biennial Observation of
17 Carbon, Acidification, Transport and Sedimentation in the North Atlantic) section is a long-term repeat
18 hydrographic transect extending from Portugal to Greenland. Since 2002, physical and biogeochemical
19 measurements have been carried out biennially along the OVIDE-BOCATS section, contributing to a better
20 understanding of water mass properties, mixing, circulation, carbon storage, and climate change impacts such as
21 ocean acidification (OA) in the NA. In particular, the high-precision pH measurements on the total hydrogen ion
22 scale (pH_T) from the OVIDE-BOCATS program represent a key milestone in monitoring OA in this particularly
23 climate sensitive region. The method used for pH_T determination relies on adding meta-cresol purple (mCP) dye to
24 the seawater sample and spectrophotometrically measuring its absorbances at specific wavelengths. The OVIDE-
25 BOCATS program has used unpurified mCP dye, which impurities have been proven to bias pH_T values. Here we
26 quantified the bias induced by these impurities in pH_T measurements. We found that measurements carried out
27 using the unpurified mCP dye tend to be, on average, **0.011 ± 0.002** pH_T units higher than those obtained using the
28 purified mCP dye, with this difference slightly decreasing at higher pH_T values. Moreover, we tested independent
29 methods to correct the effect of impurities in both the historical and recent OVIDE-BOCATS pH_T data,
30 demonstrating that the correction is consistent across methods. The long-term pH_T dataset has been updated to
31 include newly acquired data and absorbance measurements, and to standardize corrections for mCP dye impurities.
32 This effort results in a twenty-year dataset of pH_T corrected for mCP dye impurities, that demonstrates the
33 possibility of a global effort to improve the reliability and coherency of spectrophotometric pH_T measurements
34 made with unpurified mCP dye. The corrections applied to our pH_T dataset have negligible implications for the OA
35 rates previously reported, but they do affect the depth of the aragonite saturation horizon, implying a shoaling of
36 approximately 150 m. The dataset is available at <https://doi.org/10.5281/zenodo.17789895> (Pérez et al., 2025).

1 Introduction

38 The oceanic absorption of anthropogenic CO₂ (C_{ant}) is causing major changes in the marine carbonate system
 39 chemistry (Friedlingstein et al., 2023; Le Quéré et al., 2015). The ocean is slightly basic generally; however, C_{ant}
 40 uptake increases the concentration of total hydrogen ions ([H⁺]_T), decreasing pH and the concentration of carbonate
 41 ions. These changes are collectively referred to as ocean acidification (OA) (Caldeira and Wickett, 2003; Orr et al.,
 42 2005), and they are especially detrimental for calcifying marine organisms and their ecosystems (IPCC, 2019). OA
 43 is a major concern for decision-makers at both local and global scales due to its potential impacts on marine
 44 ecosystem health and food security (Gattuso et al., 2015). The future impact of OA will depend on variations in the
 45 long-term mean and the short-term temporal variability of the marine carbonate system (Kwiatkowski and Orr,
 46 2018).

47

48 Due to their physicochemical characteristics, surface waters in polar and subpolar regions are expected to
 49 experience the greatest OA impact (IPCC, 2019; Orr et al., 2005). However, the impact of OA is not limited to
 50 surface waters. Recent observations have shown that intermediate layers of the North Atlantic (NA) are
 51 experiencing higher OA rates than surface waters (Pérez et al., 2021; Resplandy et al., 2013) due to its distinctive
 52 circulation dynamics. The upper limb of the Atlantic Meridional Overturning Circulation (AMOC) transports C_{ant}
 53 from the subtropics to the Subpolar North Atlantic (SPNA), where it is transferred to intermediate and deep layers—
 54 with lower buffering capacity than surface layers—through deep winter convection and water mass formation
 55 (Asselot et al., 2024). This process would ultimately contribute to the deterioration of NA deep-water coral
 56 ecosystems (Fontela et al., 2020a; García-Ibáñez et al., 2021; Gehlen et al., 2014; Perez et al., 2018).

57

58 The demand for open-access OA data is increasing, driven by United Nations Sustainable Development Goal
 59 (SDG) 14 and by its role as a climate indicator recognized by the World Meteorological Organization (WMO).
 60 Although great progress in autonomous marine data collection has been achieved in recent years (Bushinsky et al.,
 61 2025), high-quality, ship-based pH measurements remain essential for ensuring the reliability of OA data collected
 62 by sensors on autonomous platforms, such as Argo floats and moorings, by enabling rigorous calibration protocols
 63 that correct for potential biases over time due to sensor drift, biofouling, and pressure effects (Maurer et al., 2021;
 64 Pérez et al., 2023; Takeshita et al., 2018).

65

66 Despite the critical role of pH data in understanding OA, significant limitations exist within key ocean databases
 67 such as the Global Ocean Data Analysis Project (GLODAPv2) (Olsen et al., 2016; Key et al., 2015). In
 68 GLODAPv2, pH data that is reported on the total hydrogen ion scale (pH_T)—which accounts for both the aqueous
 69 hydrogen ions (H₃O⁺) and the associated form with sulfate ions (HSO₄⁻)—and have historically been collected less
 70 frequently than other carbonate system variables, such as total alkalinity (A_T) and total dissolved inorganic carbon
 71 (C_T) (Key et al., 2015; Lauvset et al., 2024; Olsen et al., 2019). A_T and C_T measurements are generally considered
 72 more reliable due to the availability of standardized reference materials, consensually accepted methods, and
 73 quality control procedures. In contrast, although pH_T measurements are technically precise, easy to perform, and
 74 cost-effective, their intercomparability is more challenging, arising from methodological inconsistencies across
 75 various research initiatives (Dickson et al., 2015; Ma et al., 2019; Álvarez et al., 2020; Capitaine et al., 2023). The
 76 lack of traceability to a common reference, preferentially the International System of units for spectrophotometric
 77 pH measurements (Dickson et al., 2015), and the unavailability of pH reference materials within the seawater pH
 78 range (Capitaine et al., 2023), together with the documented issues affecting pH_T calculated from A_T and C_T
 79 (including pH_T-dependent offsets and larger propagated uncertainties; Álvarez et al., 2020; Carter et al., 2024b),
 80 mean that neither unadjusted direct observations nor calculated values currently provide a fully trusted global
 81 reference. Both limitations may therefore affect the reliability of pH data for climate-quality OA assessments.

82 Briefly, the spectrophotometric pH method is a straightforward technique that involves adding an acid-base
83 indicator dye to the seawater sample. The method was initially defined in the 1980s (Robert-Baldo et al., 1985;
84 Byrne and Breland 1989), and the use of meta-cresol purple (mCP) as the indicator dye began in the 1990s (Clayton
85 and Byrne, 1993). The technique has been updated since then, but it still lacks metrological traceability and
86 reference materials (Ma et al., 2019; Carter et al., 2024a). The method is based on the distinct absorbance
87 wavelengths of the indicator dye's acid and basic forms, which are used to calculate an absorbance ratio.
88 Subsequently, pH_T is calculated using the indicator dye's dissociation constant and its extinction coefficients
89 through a parameterization in function of temperature and salinity, relating the absorbance ratio with pH_T . This
90 method offers a high degree of precision (error even lower than ± 0.001 pH units), with an approximate total
91 uncertainty of ± 0.01 pH_T units (Dickson, 2010; Carter et al., 2024a). A primary source of error in these pH_T
92 measurements arises from the impurities present in the mCP dye itself (Liu et al., 2011). Over the last decade,
93 different studies proved that mCP impurities cause the measured pH_T to exhibit a bias that is dependent on the
94 sample's pH_T and the brand and batch of the mCP dye used (Liu et al., 2011; Yao et al., 2007). Consequently, mCP
95 was proposed to be purified (Liu et al., 2011; Rivaro et al., 2021) to remove these impurities and parameterizations
96 re-evaluated for those purified mCP dyes (Liu et al., 2011; Loucaides et al., 2017; Müller et al., 2018). Although
97 some laboratories, mostly in the US, currently use purified mCP dye (Carter et al., 2018), purified mCP dyes are
98 not commercially available, being scarce and expensive, and therefore not affordable for all laboratories.
99 Alternatively, it is possible to evaluate the effect of these impurities on the absorbance values and correct them
100 accordingly (Douglas and Byrne, 2017; hereafter DB'17; Takeshita et al., 2020, 2021; Woosley, 2021).
101

102 Over the past two decades, the GO-SHIP A25 OVIDE-BOCATS ship-based hydrographic section (OVIDE-
103 BOCATS hereafter; see Sect. 2.1)—the only transoceanic cruise with a biennial frequency in the CLIVAR (Climate
104 and Ocean: Variability, Predictability, and Change) and GO-SHIP programs—has built an extensive pH_T time
105 series in the NA of more than 23,500 pH_T samples measured using unpurified mCP dye. During the 11 OVIDE-
106 BOCATS cruises, pH_T was measured spectrophotometrically following a consistent methodology and using the
107 same commercial mCP dye brand, Sigma-Aldrich, which—like other commercial brands—contains impurities (Liu
108 et al., 2011; Yao et al., 2007). As awareness of pH_T biases introduced by mCP impurities has grown, so has the
109 need to assess and correct their impact to ensure the internal consistency and long-term comparability of the
110 OVIDE-BOCATS pH_T dataset. In this context, we evaluated the bias induced by these impurities by carrying out
111 measurements with purified and unpurified mCP dyes, and assessed independent methods to account for and correct
112 the effect of these impurities in both the historical and contemporary OVIDE-BOCATS pH_T data. Here we present
113 (1) the new data from the last two BOCATS cruises of 2021 and 2023, (2) the absorbance measurements along
114 with the evaluation of the impurities effect on them, and (3) the entire OVIDE-BOCATS pH_T database product
115 since 2002, consistently adjusted for impurity-related bias. This effort allowed us to evaluate—in a consistent
116 way—the OA rates in the NA and to improve the reliability of the pH_T data collected to date, which is fundamental
117 for understanding the ocean's response to climate change.
118

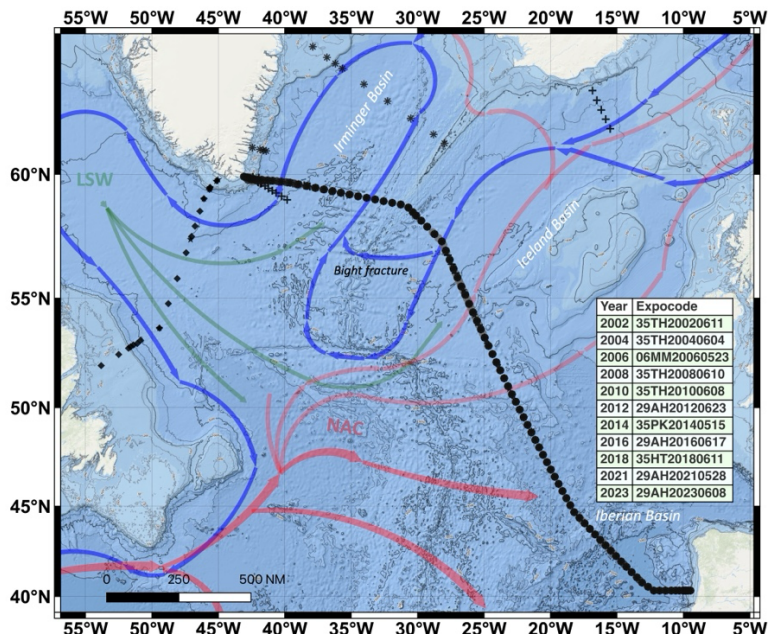
120 2. Methods

121 2.1 OVIDE-BOCATS transoceanic section

122 The OVIDE-BOCATS section is a high-quality hydrographic transect in the NA, extending from Portugal to
123 Greenland and largely following the GO-SHIP A25 track (Fig. 1), with the objective of studying the SPNA region.
124 Initially focused on physical oceanography (Mercier et al., 2024), its scope rapidly expanded to include critical

125 aspects of the carbon cycle, such as OA and the uptake and storage of C_{ant} in the SPNA—one of the ocean's largest
126 C_{ant} reservoirs (Sabine et al., 2004). Since 2002, in situ physical and on-board biogeochemical measurements have
127 been performed biennially along the OVIDE-BOCATS section. This repeated section is one of the longest-standing
128 and most frequently revisited transects within the GO-SHIP and CLIVAR programs. Accordingly, data
129 management follows strict policies, and all datasets are publicly available
130 (https://www.ncei.noaa.gov/access/ocean-carbon-acidification-data-system/oceans/RepeatSections/clivar_ovide.html).
131

132 Thanks to its high frequency of repeated occupations, the OVIDE-BOCATS dataset offers a unique opportunity to
133 study the biennial evolution of NA processes. The program focuses on water mass properties, mixing, and
134 circulation; the impact of climate events on NA dynamics; volume and heat transports; and AMOC variability.
135 Particular attention is given to investigate key water masses such as Subpolar Mode Water (SPMW) and Labrador
136 Sea Water (LSW)—both formed through deep winter mixing in the SPNA—as well as Denmark Strait Overflow
137 Water (DSOW) and Iceland-Scotland Overflow Water (ISOW)—both resulting from the entrainment of SPMW
138 and LSW into the overflows at the sills between Greenland, Iceland, and Scotland, respectively (García-Ibáñez et
139 al., 2015; Lherminier et al., 2010).
140



142
143 **Figure 1.** Bathymetric map showing the main water masses and circulation patterns within the SPNA region
144 covered by the OVIDE-BOCATS program (station locations indicated by black dots). Stations outside the main
145 OVIDE-BOCATS (A25) section are opportunistic stations, dependent on the ship's route, whose data are also
146 included in the final database product: "plus" symbols near Iceland and Greenland are stations sampled in 2006;
147 "pentagon" and "rhombus" located in the Labrador Sea are stations sampled during 2012 and 2014 cruises; and
148 "asterisk" symbols are stations sampled in 2023, near Greenland and in the Irminger Sea. The inset table lists each
149 biannual cruise along with its corresponding expocode as identified in GLODAP. Major currents and water masses
150 are illustrated in different colors according to their temperature and depth (from red—warmer and shallower—to
151 blue—colder and deeper). The main schematized currents and water masses include the North Atlantic Current

152 (NAC), Labrador Sea Water (LSW), and Iceland-Scotland Overflow Water (ISOW). The principal basins traversed
153 along the OVIDE-BOCATS section, from west to east, are the *Irminger*, *Iceland*, and *Iberian basins*.

154 Research within the OVIDE-BOCATS framework has also focused on carbon inventories and the deep
155 biogeochemical imprint, such as the role of the Deep Western Boundary Current (DWBC) in transporting oxygen,
156 nutrients, and dissolved organic carbon (Álvarez-Salgado et al., 2013; Fontela et al., 2019; 2020b). In addition,
157 OVIDE-BOCATS has evaluated OA rates in the NA (Fontela et al., 2020a; García-Ibáñez et al., 2016; Vázquez-
158 Rodríguez et al., 2012) and analyzed its impact on marine biodiversity (Pérez et al., 2018; García-Ibáñez et al.,
159 2021) as well as the ocean's capacity to absorb, store, and transport CO₂ (Bajon et al., 2025, manuscript in review;
160 Pérez et al., 2013; Zunino et al., 2015). In summary, the sustained observations from the OVIDE-BOCATS program
161 demonstrated to be essential for detecting OA trends, improving climate models, and understanding the SPNA's
162 response to climate change (DeVries et al., 2023; Rodgers et al., 2023).

163 **2.2 pH_T determination**

164 **2.2.1 Spectrophotometric pH_T method fundamentals**

165 In all OVIDE-BOCATS cruises, pH_T was measured manually following the spectrophotometric method proposed
166 by Clayton and Byrne (1993)—hereafter CB'93. This method involves adding a mCP dye solution to the seawater
167 sample and calculating the sample's pH_T using the following equation:

$$169 \quad \text{pH}_T = \text{pK}_2 + \log_{10} \left(\frac{[\text{I}^2]}{[\text{HI}^-]} \right) \quad (1),$$

170 where $[\text{HI}^-]$ and $[\text{I}_2^-]$ represent the concentrations of mono-dissociated and bi-dissociated species of the indicator
171 dye, respectively. The concentration ratio ($[\text{I}^2] / [\text{HI}^-]$) can be determined spectrophotometrically by measuring
172 absorbance at the corresponding maximum absorbance wavelengths (A), i.e., 434 nm and 578 nm, respectively,
173 corrected for baseline absorbance at 730 nm—hereafter referred to as ₄₃₄A, ₅₇₈A, and ₇₃₀A, respectively. pH_T is then
174 calculated using CB'93 parameterization of Eq. (1):
175

$$176 \quad \text{pH}_T = 1245.69/T + 3.8275 + (2.11 \cdot 10^{-3}) \cdot (35 - S) + \log \left(\frac{(R - 0.0069)}{(2.222 - 0.133 \cdot R)} \right) \quad (2),$$

177 where T is temperature in Kelvin, S is salinity, and R is the ratio of the absorbances of the mono-dissociated and
178 bi-dissociated forms of the indicator dye corrected for baseline absorbance:

$$180 \quad R = \frac{(\text{578A} - \text{730A})}{(\text{434A} - \text{730A})} \quad (3).$$

182 The first three terms of Eq. (2) represent the second dissociation constant of mCP dye (pK_2 , or $-\text{pK}_1$ in CB'93). The
183 $-\text{pK}_1$ obtained by CB'93 is based on the *TRIS* buffer characterization of Dickson (1993), which used electromotive
184 force data from Ramette et al. (1977; Lee et al., 2000). DelValls and Dickson (1998)—hereafter DVD'98—later
185 determined that the pH_T values assigned to *TRIS* buffers needed to be increased by 0.0047, for all temperatures and
186 salinities. These corrected *TRIS* pH_T values have recently been confirmed by Müller et al. (2018). Consequently,
187 spectrophotometric pH_T values obtained using the CB'93 parameterization should be adjusted by +0.0047 pH_T units
188 (DVD'98; Lee et al., 2000).

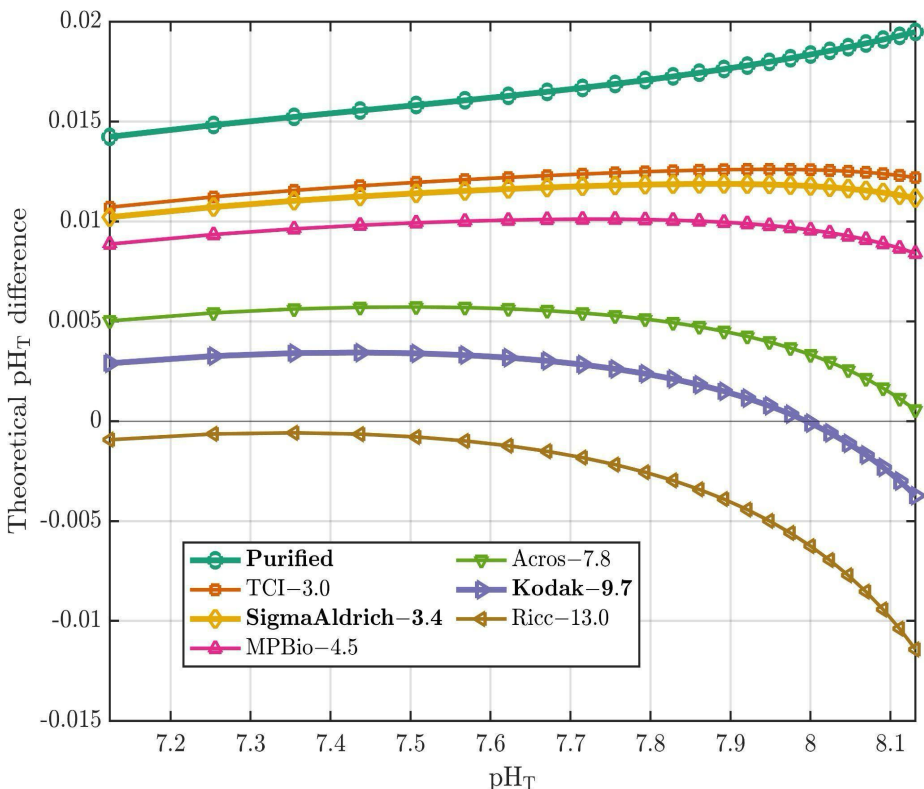
189 The CB'93 parameterization was developed using Kodak mCP dye, prepared in deionized water, which contained
190 impurities contributing significant absorbance at 434 nm (referred to as ₄₃₄A_{imp}). However, it was not until the 2000s
191 that the impact of impurities on pH_T measurements was evidenced. Specifically, Yao et al. (2007) compared pH_T

193 determinations using Sigma-Aldrich and Kodak mCP dyes with *TRIS* buffers, finding that pH_T values obtained
194 with Sigma-Aldrich mCP dye were between 0.001 to 0.006 pH_T units higher than those with Kodak mCP dye (for
195 pH_T ranging from 7.4 to 8.2), attributed to lower $_{434}\text{A}_{\text{imp}}$ values in the Sigma-Aldrich mCP dye. Later, Liu et al.
196 (2011; hereafter L'11) purified mCP dye and developed a new parameterization to determine pH_T from R ,
197 demonstrating that applying their new parameterization to R data measured with impure mCP dye results in pH_T
198 values up to 0.018 pH_T units lower. Subsequently, Loucaides et al. (2017) and Müller et al. (2018) produced very
199 similar parameterizations, extending the valid salinity and temperature ranges and confirming the same pH_T versus
200 R relationship at 25°C and oceanic salinities (see Fig. S1 in Álvarez et al., 2025). Thus, ideally, pH_T measurements
201 should be performed using purified, well-characterized mCP dyes and following a consensus method that ensures
202 traceability to the International System of Units (SI; Capitaine et al., 2023). However, the purification procedure is
203 not accessible to many laboratories routinely measuring seawater pH_T . To overcome this limitation and facilitate
204 high-quality spectrophotometric pH_T measurements, DB'17 proposed a method to determine $_{434}\text{A}_{\text{imp}}$ and an
205 associated correction procedure. This approach allows R to be corrected for the contribution of impurities at $_{434}\text{A}$
206 (i.e., $_{434}\text{A}_{\text{imp}}$), and consequently enables pH_T calculations using parameterizations derived for purified mCP dye,
207 such as the L'11 parameterization.
208

209 What is the bias introduced in pH_T measurements as a result of mCP dye impurities? Most of the spectrophotometric
210 pH_T values in GLODAPv2 (Lauvset et al., 2024) are calculated using the CB'93 parameterization, based on
211 measurements made with mCP dyes that contain impurities. Figure 2 shows a family of curves representing the
212 theoretical differences between pH_T values calculated using the CB'93 parameterization with R values that would
213 have been obtained with unpurified mCP dyes (i.e., with varying $_{434}\text{A}_{\text{imp}}$), and those obtained using the L'11
214 parameterization applied to R values corresponding to a fully purified mCP dye (i.e., $_{434}\text{A}_{\text{imp}} = 0$). We computed
215 the corresponding $_{434}\text{A}$ values ($_{434}\text{A}_{\text{pur}}$, i.e., $_{434}\text{A}_{\text{imp}} = 0$) using the relationship described in Sect. 2.2.4 for a set of
216 theoretical purified R (R_{pur}) values ranging from 0.3 to 2.6. Both the purified R values and their associated $_{434}\text{A}$
217 values were then used in Eq. (11) of DB'17 to compute the adjusted R values (R_{unpur} ; referred to as R_{obs} in DB'17)
218 that reflect the contribution of mCP dye impurities ($_{434}\text{A}_{\text{imp}} \neq 0$) as follows:
219

$$R_{\text{unpur}} = R_{\text{pur}} / (1 + (_{434}\text{A}_{\text{imp}} / _{434}\text{A}_{\text{pur}})) \quad (4).$$

220 The mCP dye brands and their corresponding absorbance values due to their impurities, as shown in Fig. 2, are
221 primarily taken from Table 2 of DB'17, that are based on an mCP dye concentration of 3.3 μM in the sample cell.
222 When the CB'93 parameterization is applied to R_{pur} ($_{434}\text{A}_{\text{imp}} = 0$) at $S = 35$ and 25°C, the largest theoretical pH_T
223 differences (> 0.015 pH_T units) are observed relative to pH_T values obtained by applying the L'11 parameterization
224 to the corresponding R_{pur} under the same conditions (see turquoise line in Fig. 2). In contrast, when CB'93
225 parameterization is applied to R_{unpur} values obtained with Kodak mCP dye, the resulting pH_T values differ by only
226 ± 0.003 pH_T units from those obtained with the L'11 parameterization with a purified mCP dye, with minimal
227 differences observed in the pH_T range of 7.65 to 8.15 (purple line in Fig. 2). This agreement arises because the
228 CB'93 parameterization—developed using Kodak mCP dye and calibrated against *TRIS* buffers using unpurified
229 mCP dye—yields lower R values than that obtained with purified mCP dye. As a result, both parameterizations
230 converge around the *TRIS* buffer pH_T value (8.093 at 25°C; DVD'98). Indeed, Fig. 2 shows that larger biases in the
231 final pH_T arise when using the CB'93 parameterization with mCP dyes with lower impurity content, while the
232 magnitude and pH_T -dependence of these biases increases with higher impurity levels.
233



236 **Figure 2.** Theoretical differences in pH_T (y-axis) between values using the CB'93 parametrization with the DVD'98
 237 correction (applied to R values derived from mCP dyes with varying impurities) and those calculated using the
 238 L'11 parametrization (applied to R values derived from a purified mCP dye). The differences are plotted against
 239 pH_T computed using the L'11 parameterization (x-axis), at $S = 35$ and $T = 25^\circ\text{C}$. Each mCP dye is represented by
 240 a different color, with its corresponding ${}_{434}\text{A}_{\text{imp}}$ value (in units of 10^{-3} absorbance) specific to the lot used in DB'17,
 241 listed after the indicator dye name. **Bold** indicates mCP dye brands discussed in this work. All ${}_{434}\text{A}_{\text{imp}}$ values are
 242 taken from DB'17 and are specific to the lot used, except for Sigma-Aldrich, whose value was determined in this
 243 study.
 244

245 **2.2.2 pH_T sampling and manual spectrophotometric procedure during the OVIDE-BOCATS cruises**

246 On all OVIDE-BOCATS cruises, seawater samples for pH_T were collected after oxygen samples, using 100 mm
 247 pathlength cylindrical optical glass cells with two stoppers (Dickson et al., 2007). Each sample was taken by rinsing
 248 the optical cell twice and flushing it with seawater two or three times its volume, ensuring no air bubbles remained.
 249 To achieve this, the cell was held with the outlet above the inlet, the outlet was plugged first, the sampling tube
 250 was removed, and the second plug was inserted—taking care to avoid air bubbles. After rinsing and externally
 251 drying the cells, they were placed in a thermostatic incubator set at 25°C for at least 30–45 minutes to ensure
 252 temperature stabilization at 25°C prior to their measurement.
 253

254 For each sample, a blank measurement was performed after drying and cleaning both faces of the optical cell and
 255 placing it in the spectrophotometer's cell holder. Following blanking at the three target wavelengths (434 nm, 578
 256 nm, and 730 nm) with sampled seawater, 75 μL of 2 mM mCP dye solution were added to each 28 mL sample cell
 257 using an adjustable repeater pipette (SOCOREX), resulting in a final mCP dye concentration of 5.36 μM in the

258 cell. Dispenser syringes were wrapped in aluminum foil to prevent photodegradation of the mCP dye (Fontela et
259 al., 2023). After the mCP dye addition, the cell was thoroughly shaken and placed back in the holder in the same
260 orientation as for the blanking, and triplicate absorbance readings were carried out at the same target wavelengths
261 as for the blank. All absorbance readings were carried out in the spectrophotometer's thermostatted cell
262 compartment, maintained at $25.0 \pm 0.2^\circ\text{C}$.
263

264 Byrne and Breland (1989) demonstrated that R measurements are largely insensitive to small temperature
265 variations, for cresol red dye. The same general behaviour applies to mCP dye, in which R values between 0.5 and
266 2.8 exhibit pH_T errors of less than 0.001 pH_T units per 1°C change when using the L'11 parameterization. This
267 insensitivity arises because, for mCP, the temperature dependence of the indicator dye's pK_2 closely parallels the
268 temperature dependence of seawater pH. The CB'93 parametrization shows a slightly greater temperature
269 sensitivity, such that temperature deviations must be kept within approximately $\pm 0.5^\circ\text{C}$ to limit the pH_T error to \leq
270 0.0012 pH_T units. Therefore, it is recommended to ensure that temperature deviations remain within $\pm 0.5^\circ\text{C}$ of the
271 reference temperature (25°C). In our procedure, sample temperature was monitored every five measurements to
272 verify that it remained within this tolerance.
273

274 **2.2.3 Effect of the indicator dye addition and spectrophotometer performance on the pH_T measurements**

275

276 Throughout the OVIDE-BOCATS program, the mCP dye used was from Sigma-Aldrich (Cat. No. 11,436-7 in the
277 basic form; $\text{C}_{21}\text{H}_{17}\text{NaO}_5\text{S}$; molecular weight 404.41 g), with only a few different batches from this brand used over
278 the 11 cruises. Prior to 2018, mCP dye solutions were prepared by dissolving 0.080 g of the mCP sodium salt in
279 100 mL of natural seawater. Following DB'17 recommendations, the preparation method was modified in 2018,
280 with the mCP dye being dissolved in 0.7 M NaCl instead of seawater. The absorbances of the mCP dye solutions
281 at 434 nm, 578 nm, and 730 nm were measured spectrophotometrically using a 0.1 mm optical cell to ensure that
282 the R values remained close to 1, corresponding to a pH_T of approximately 7.67 (Li et al., 2020; at $\text{S} = 35$ and $\text{T} =$
283 25°C). mCP dye solutions were stored in Pyrex bottles, refrigerated, and protected from light using aluminum foil.
284

285 The addition of the indicator dye slightly perturbs the sample's pH_T , with the magnitude of this effect increasing
286 for shorter optical pathlengths and when the pH_T difference between the sample and the indicator dye is large
287 (Chierici et al., 1999). For instance, when using a 100 mm optical pathlength, the indicator dye induced pH_T
288 perturbation is typically less than 0.006 pH_T units within the pH_T range of 7.6 to 8.0 (Chierici et al., 1999; Li et al.,
289 2020; Table 1), which is relatively minor but not negligible. A common approach to account for this effect, as
290 proposed by CB'93, involves performing a double addition of the indicator dye solution to the samples and
291 calculating the difference in the resulting R values (ΔR) between the first (single) and second (double) addition.
292 This ΔR correction is then applied to the measured R values. Alternatively, the correction can be expressed in terms
293 of ΔpH_T , which may be directly applied to the computed pH_T values (Takeshita et al., 2020, 2022). Both ΔR and
294 ΔpH_T correction approaches were evaluated. During each cruise, between two and four double indicator dye
295 addition experiments were performed. In each experiment, seawater samples were modified to obtain four pH_T
296 values ranging from 7.4 to 8.2, with four samples per pH_T level ($\text{N} = 16$ samples per experiment). Following
297 blanking, an initial addition of 50 μL of mCP dye solution was made to each sample, and absorbance was measured
298 as described in Section 2.2.2. A second addition of 50 μL of mCP dye solution was then made (resulting in a total
299 of 100 μL of mCP dye solution added), and absorbance measurements were repeated. These double-addition
300 experiments enabled the determination of linear regressions of the change in pH_T ($\Delta \text{pH}_T = \text{pH}_{T,2} - \text{pH}_{T,1}$; where
301 subscripts 2 and 1 refer to 100 μL and 50 μL of mCP dye solution added, respectively) or R ($\Delta R = R_2 - R_1$) as a
302 function of the initial $\text{pH}_{T,1}$ or R_1 , respectively (Fig. S1 in the Supplement). This two-step 50 μL addition bracketed

303 the typical 75 μL reference volume added to the sample, allowing us to evaluate the dye effect on the ΔR or ΔpH_T
304 both below and above this reference. The corresponding relationship was expressed as:
305

$$306 \quad \Delta \text{pH}_T = a \cdot (\text{pH}_T - \text{pH}_T^{y=0}) \quad (5),$$

307

308 where a is the slope of the linear regression and $\text{pH}_T^{y=0}$ represents the pH_T at which the indicator dye addition has
309 no effect. An analogous expression was used for ΔR [$\Delta R = a' \cdot (R - R^{y=0})$, being a' the particular slope for the ΔR -
310 R linear regression]. Since the standard volume of mCP dye solution used in OVIDE-BOCATS cruises was 75 μL ,
311 while the double addition experiments used 50 μL additions, a correction factor of 75/50 was applied to adjust both
312 ΔpH_T and ΔR . The corrected pH_T ($\text{pH}_{T,\text{corrected}}$) was thus calculated as:
313

$$314 \quad \text{pH}_{T,\text{corrected}} = \text{pH}_m - 75/50 \cdot a \cdot (\text{pH}_m - \text{pH}_T^{y=0}) \quad (6),$$

315

316 where pH_m is the uncorrected measured pH_T (i.e., prior to its ΔpH_T correction) [analogously: $R_{\text{corrected}} = R - 75/50 \cdot$
317 $a' \cdot (R_m - R^{y=0})$]. At $\text{pH}_T^{y=0}$, the R (pH_T) of the original sample and the R (pH_T) of the indicator dye are the same,
318 so no change is observed. If $\text{pH}_m > \text{pH}_T^{y=0}$, then $\text{pH}_{T,2}$ (or R_2) $<$ $\text{pH}_{T,1}$ (or R_1), as the mCP dye addition lowers pH_m ;
319 hence, $\text{pH}_{T,\text{corrected}}$ will be higher than pH_m . Conversely, if $\text{pH}_m < \text{pH}_T^{y=0}$, the mCP dye addition increases the pH_m ,
320 and $\text{pH}_{T,\text{corrected}}$ will be lower than pH_m .
321

322 The linear regressions of ΔR versus R_1 (ΔR -vs- R_1) and ΔpH_T versus $\text{pH}_{T,1}$ (ΔpH_T -vs- $\text{pH}_{T,1}$) obtained for each
323 OVIDE-BOCATS cruise are summarized in Table 1. The slopes for ΔR -vs- R_1 range from 0.0048 (BOCATS2-
324 2023 cruise) to 0.0230 (OVIDE-2006 cruise), with the perturbation vanishing ($\Delta R = 0$) when $R \approx 1.0 \pm 0.2$, i.e.,
325 when the sample pH_T closely matches that of the mCP dye solution. Carter et al. (2013) proposed a methodological
326 refinement by normalizing ΔR with the change in absorbances at the isosbestic point ($\Delta_{488\text{A}}$; see Section 2.2.4),
327 improving the robustness of the correction. Accordingly, using the Carter et al. (2013) approach [$\Delta(R/_{488\text{A}})$ versus
328 R_1 ; $\Delta(R/_{488\text{A}})$ -vs- R_1] increased the overall explained variability (R^2) of the linear fits. Similarly, for ΔpH_T -vs- $\text{pH}_{T,1}$
329 regressions, the smallest slope was recorded for BOCATS2-2021 cruise and the largest again in the OVIDE-2006
330 cruise (Table 1). When using $\Delta(\text{pH}_T/_{488\text{A}})$ -vs- $\text{pH}_{T,1}$, the distribution of regression slopes was similar but less
331 variable (average regression: $-0.0431 \pm 0.019 \cdot (\text{pH}_T - 7.73 \pm 0.09)$; Table 1), consistent with the mCP dye
332 perturbation trends reported by Takeshita et al. (2022) [$\Delta \text{pH}_T/\Delta_{488\text{A}} = -0.042 \pm 0.003 \cdot (\text{pH}_T - 7.76)$; $N = 91$]. The
333 OVIDE-BOCATS pH_T data were corrected using the cruise-specific $\Delta \text{pH}_T/\Delta_{488\text{A}}$ relationships. Overall, the
334 evaluation of the mCP dye's perturbation on the sample's pH_T was consistent across all cruises, regardless of
335 whether ΔR - or ΔpH_T -based methods were used.
336

337 In addition to the impact of the mCP dye addition, both the ΔR and ΔpH_T corrections can be influenced by the
338 performance characteristics of the spectrophotometer used (Carter et al., 2013; Álvarez et al., 2020; Takeshita et
339 al., 2021; Fong et al., 2024). If the spectrophotometer follows the Beer-Lambert law (i.e., no optical non-linearity),
340 the effect of the mCP dye addition results in a linear relationship for both ΔR -vs- R_1 and ΔpH_T -vs- $\text{pH}_{T,1}$ regressions
341 (Li et al., 2020), meaning that the relationships are only affected by chemistry. This only-chemical effect was
342 evaluated by Li et al. (2020) over a wide range of salinities and A_T s, including those present during OVIDE-
343 BOCATS cruises, allowing us to replicate their chemical model (blue diamonds in Fig. 3). The ΔR -vs- R_1 regression
344 exhibits better linearity than ΔpH_T -vs- $\text{pH}_{T,1}$ regression, though both reflect the mCP dye's interference in the
345 physico-chemical ionic equilibrium of the marine carbonate system. However, when introducing a 0.04% deviation
346 from linearity in the spectrophotometer (i.e., loss of the Beer-Lambert behavior, thus including an additional impact
347 to the chemical effect) the regression slopes for both ΔpH_T -vs- $\text{pH}_{T,1}$ and ΔR -vs- R_1 roughly double, revealing that

348
349
350
351
352
353

this instrumental non-linearity amplifies the chemistry effect of the mCP dye. Notably, while ΔpH_T remains linear during this distortion, ΔR becomes non-linear (orange squares in Fig. 3). When $R = 1$ (i.e., $_{434}\text{A} = 578\text{A}$ and sample $\text{pH}_T = \text{mCP dye pH}_T$), non-linearity impacts both absorbances equally, resulting in no change in R and therefore in pH_T . In contrast, deviations from $R = 1$ (or $\text{pH}_T = 7.65$; at $S = 35$ and $T = 25^\circ\text{C}$) enhance this artifact due to increasingly unequal absorbances at $_{434}\text{A}$ and 578A , leading to spurious R values and biased pH_T .

354
355
356
357
358
359
360
361

Table 1. Summary of each OVIDE-BOCATS cruise alias, the spectrophotometer used, and the mean and standard deviation of $_{488}\text{A}$ values (from 2002 to 2018 estimated using Eq. (7), from 2018 to 2023 directly measured). The table also includes the linear regression equations and their explained variance (R^2) for the ΔR -vs- R_1 , $\Delta(R/_{488}\text{A})$ -vs- R_1 , ΔpH_T -vs- $\text{pH}_{T,1}$, and $\Delta(\text{pH}_T/_{488}\text{A})$ -vs- $\text{pH}_{T,1}$ relationships. Additionally, it reports the corresponding ΔpH_T at $\text{pH}_T = 7.7$ and $\text{pH}_T = 8.0$, calculated using the $\Delta(\text{pH}_T/_{488}\text{A})$ -vs- $\text{pH}_{T,1}$ relationship for each cruise. Note that ΔR -vs- R_1 and ΔpH_T -vs- $\text{pH}_{T,1}$ regressions are based on an addition of 50 μL mCP dye solution; therefore, a correction factor (e.g., 75/50) must be applied when using ΔR -vs- R_1 and ΔpH_T -vs- $\text{pH}_{T,1}$ relationships to samples measured with a different addition volumes (e.g., 75 μL).

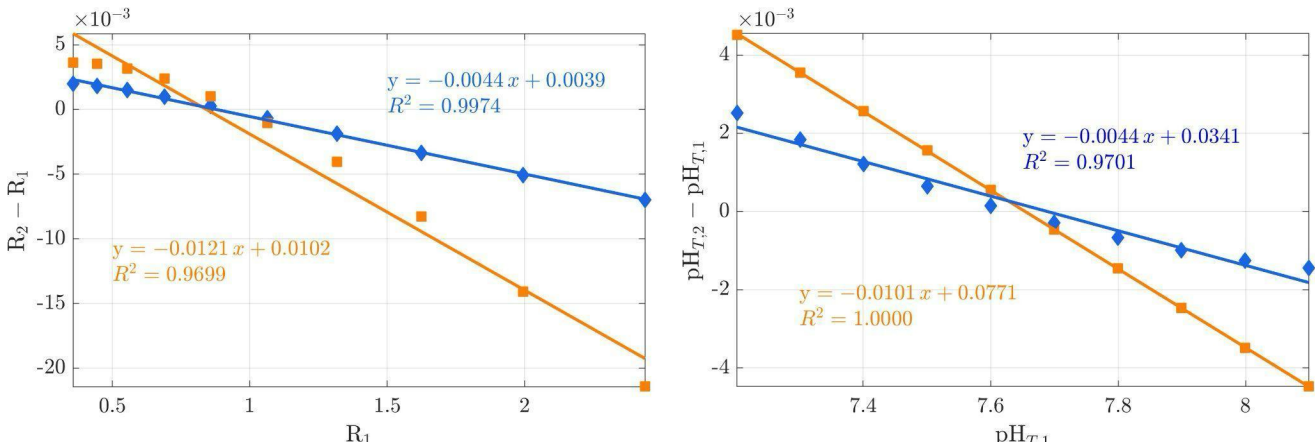
CRUISE	Spectrophotometer	$_{488}\text{A}$	ΔR -vs- R_1 R^2	$\Delta(R/_{488}\text{A})$ -vs- R_1 R^2	ΔpH_T -vs- $\text{pH}_{T,1}$ R^2	$\Delta(\text{pH}_T/_{488}\text{A})$ -vs- $\text{pH}_{T,1}$ R^2	ΔpH_T at~7.7	ΔpH_T at~8.0
Ovide-2002	CECIL-3041	0.331±0.020	-0.0068·(R-0.82) 0.32	-0.059·(R-1.07) 0.41	-0.0078·(pH _T -7.71) 0.51	-0.056·(pH _T -7.71) 0.59	0.000	0.005
Ovide-2004	Shimadzu UV-2401PC	0.232±0.020	-0.0092·(R-0.96) 0.78	-0.038·(R-0.97) 0.81	-0.0078·(pH _T -7.70) 0.70	-0.033·(pH _T -7.70) 0.73	0.000	0.002
Ovide-2006	Shimadzu UV-2401PC	0.250±0.023	-0.035·(R-1.10) 0.92	-0.134·(R-1.00) 0.94	-0.023·(pH _T -7.70) 0.88	-0.103·(pH _T -7.68) 0.96	0.001	0.008
Ovide-2008	Shimadzu UV-2401PC	0.230±0.015	-0.0060·(R-1.2) 0.60	-0.029·(R-1.04) 0.84	-0.0084·(pH _T -7.83) 0.89	-0.037·(pH _T -7.84) 0.89	-0.001	0.001
Ovide-2010	Shimadzu UV-2401PC	0.233±0.015	-0.022·(R-1.06) 0.78	-0.096·(R-1.06) 0.81	-0.0106·(pH _T -7.68) 0.70	-0.069·(pH _T -7.68) 0.73	0.000	0.005
CATARINA-2012	Perkin Elmer Lambda 800 UV-VIS	0.211±0.016	-0.014·(R-0.80) 0.93	-0.100·(R-0.81) 0.94	-0.0090·(pH _T -7.55) 0.89	-0.065·(pH _T -7.58) 0.93	0.002	0.006
Geovide-2014	Shimadzu UV-2401PC	0.218±0.007	-0.0066·(R-1.12) 0.76	-0.046·(R-1.16) 0.75	-0.0082·(pH _T -7.77) 0.76	-0.065·(pH _T -7.77) 0.71	-0.001	0.003
BOCATS-2016	Perkin Elmer Lambda 800 UV-VIS	0.369±0.022	-0.0070·(R-1.19) 0.81	-0.028·(R-1.19) 0.81	-0.0080·(pH _T -7.85) 0.91	-0.033·(pH _T -7.85) 0.91	-0.002	0.002
Ovide-2018	Shimadzu UV-2401PC	0.358±0.027	-0.0108·(R-1.09) 0.72	-0.046·(R-1.04) 0.77	-0.0083·(pH _T -7.73) 0.69	-0.030·(pH _T -7.76) 0.70	-0.001	0.003
BOCATS2-2021	Perkin Elmer Lambda 800 UV-VIS	0.359±0.027	-0.0070·(R-1.16) 0.96	-0.027·(R-1.16) 0.96	-0.0050·(pH _T -7.76) 0.89	-0.021·(pH _T -7.76) 0.90	0.000	0.002
BOCATS2-2023	Perkin Elmer Lambda 800 UV-VIS	0.389±0.032	-0.0048·(R-1.12) 0.92	-0.020·(R-1.12) 0.92	-0.0063·(pH _T -7.80) 0.95	-0.023·(pH _T -7.76) 0.96	-0.001	0.002

362
363

These results suggest that the ΔpH_T -vs- $\text{pH}_{T,1}$ relationship provides a more accurate assessment of the mCP dye's effect on the sample's pH_T when the spectrophotometer exhibits even slight deviations from the Beer-Lambert law. Indeed, the small differences between the slopes of the ΔR -vs- R_1 and ΔpH_T -vs- $\text{pH}_{T,1}$ regressions reported in Table 1 can be attributed to the distinct ways in which pH_T and R respond to such nonlinearity. The theoretical slopes of ΔpH_T -vs- $\text{pH}_{T,1}$ shown in Fig. 3 are consistent with those derived experimentally (Table 1). The steepest experimental slopes observed during the cruises may reflect greater deviations from the Beer-Lambert law, which can depend on both the spectrophotometer used and the pH_T range of the seawater batches used in these assessments. Conversely, cruises with ΔpH_T -vs- $\text{pH}_{T,1}$ slopes closer to the chemical model prediction—such as in the 2021 and 2023 cruises—indicate better spectrophotometer performance. Nevertheless, the differences in $\text{pH}_{T,\text{corrected}}$ when applying either ΔR -vs- R_1 or ΔpH_T -vs- $\text{pH}_{T,1}$ corrections remain small (< 0.001 pH_T units; see Fig. S2 in the Supplement), implying that the choice of correction method has minimal impact on the final estimation of the mCP dye perturbation. For consistency, OVIDE-BOCATS pH_T data were corrected using the $\Delta\text{pH}_T/\Delta_{488}\text{A}$ approach specific to each cruise.

376

377



378 **Figure 3.** Theoretical evaluation of the difference of the impact of mCP dye perturbation on the sample's pH_T ($S = 35$; $T = 25^\circ\text{C}$; $A_T = 2300 \mu\text{mol kg}^{-1}$), depending on whether the spectrophotometer behaves linearly—i.e., follows the Beer-Lambert law—or not. The left and right panels depict the ΔR -vs- R_1 and ΔpH_T -vs- $\text{pH}_{T,1}$ relationships, respectively. Blue diamonds represent an ideal, linear spectrophotometer response, derived from the chemical model of Li et al. (2020) based on single and double additions of 50 μL of mCP dye solution ([2 mM]) to a 28 mL sample cell with a 10 cm pathlength ($_{488}\text{A} = 0.242$), assuming a pH_T of the mCP dye solution of 7.65). Orange squares incorporate an attenuation factor of 0.04% to simulate a deviation from linearity, thus representing the combined effect of spectrophotometer non-linearity and perturbation in the physico-chemical ionic equilibrium.

387 2.2.4 Absorbance at the isosbestic point

388 During the OVIDE-BOCATS cruises, mCP dye was manually added to samples using an adjustable repeater pipette
 389 (see Section 2.2.2). For each cruise, volume deviations associated with manual addition were assessed by
 390 comparing each sample to the cruise-specific mean $_{488}\text{A}$, computed from all field-layer samples (~2000 per cruise).
 391 Manual addition resulted in volume deviations exceeding 20% in approximately 3% of the samples (~ 706 cases),
 392 potentially affecting ΔR and ΔpH_T determinations. To address variability in the volume of mCP dye solution added,
 393 Carter et al. (2013) recommended measuring absorbance at the isosbestic point ($_{488}\text{A}$), which provides a reliable
 394 proxy for actual mCP dye concentration in the sample cell. Accurate quantification of the mCP dye concentration
 395 is particularly important when applying the DB'17 methodology for impurity correction, since the $_{434}\text{A}_{\text{imp}}$ value is
 396 directly proportional to the mCP dye content. Therefore, sample-specific estimates of mCP dye concentration via
 397 $_{488}\text{A}$ allow for a more precise estimate of the $_{434}\text{A}_{\text{imp}}$ value.

398 Since 2018, OVIDE-BOCATS cruises have incorporated measurements at $_{488}\text{A}$ following the recommendation by
 399 Carter et al. (2013). The additions of 75 μL of 2 mM mCP dye solution to 28 mL seawater sample resulted in
 400 averaged $_{488}\text{A}$ values of 0.359 ± 0.027 ($N = 2,193$), 0.358 ± 0.027 ($N = 2,154$), and 0.377 ± 0.032 ($N = 2,342$)
 401 during the 2018, 2021, and 2023 cruises, respectively. These averages were not statistically different from one
 402 another, resulting in a $_{488}\text{A}$ mean value of 0.370 ± 0.033 for the period 2018–2023. This $_{488}\text{A}$ mean value was used
 403 to derive a parameterization for estimating $_{488}\text{A}$ from R values, fitted for an mCP dye concentration in the cell of
 404 5.36 μM —particularly useful for pre-2018 cruises, where $_{488}\text{A}$ was not measured. For these earlier cruises, $_{488}\text{A}$
 405 was estimated using the following parameterization:
 406

$$_{488}\text{A} = 578\text{A} \cdot (-2.5486 R^{2.5} + 17.338 R^2 - 46.779 R^{1.5} + 63.109 R - 43.393 R^{0.5} + 12.962) \quad (7).$$

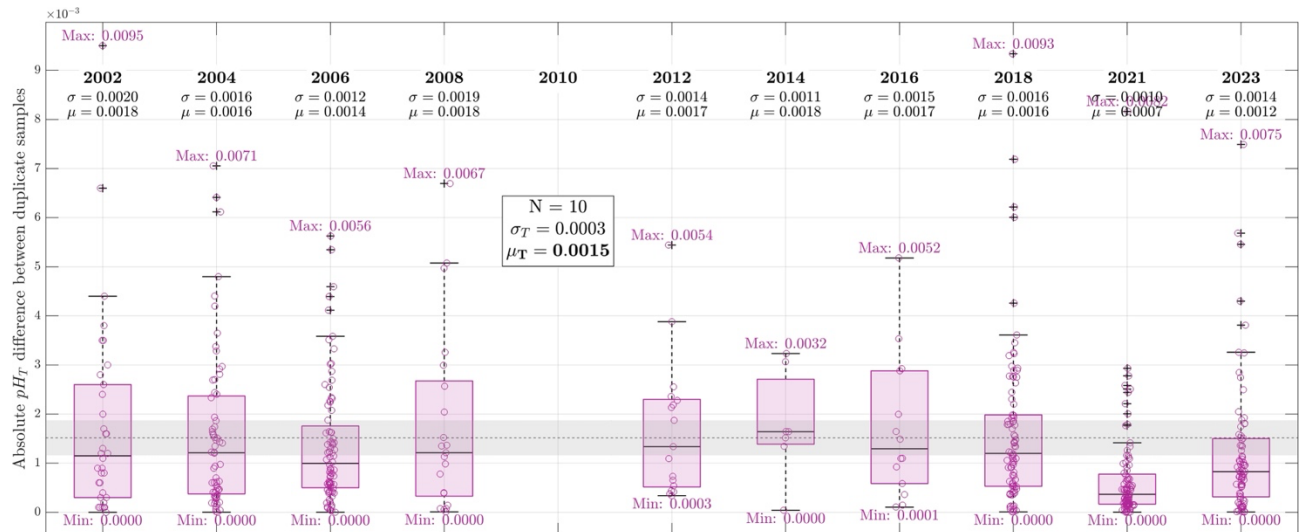
410 This fit, based on 6,910 samples from the 2018, 2021, and 2023 cruises (Fig. S3 in the Supplement), explained
 411 98.9% of the variance ($R^2 = 0.989$) and reproduces $_{488}\text{A}$ with a mean error of 0.002 ± 0.010 . It enabled a more
 412 accurate estimation of mCP dye concentrations across all cruises and improved the assessment of mCP dye impurity
 413 effects on $_{434}\text{A}$ (see Sect. 3.4). Additionally, it enhanced the accuracy of mCP dye perturbation corrections using
 414 $\Delta\text{R}/_{488}\text{A}$ and $\Delta\text{pH}_\text{T}/_{488}\text{A}$ (Table 1). A simplified parameterization using $_{434}\text{A}$ (e.g., $_{434}\text{A} = -0.0747 \cdot \text{R} + 0.403$ for 3.3
 415 μM mCP dye concentration in the sample cell) is possible, but requires correction for $_{434}\text{A}_\text{imp}$.

416 2.2.5 pH_T measurement repeatability

417 Throughout the 11 OVIDE-BOCATS cruises, a total of 502 duplicate samples were collected to evaluate the
 418 reproducibility of pH_T measurements using an unpurified mCP dye. At selected stations, two Niskin bottles were
 419 closed at the same depth to obtain replicates. Any uncertainty introduced by collecting duplicates on two different
 420 Niskin bottles (e.g., small leaks, biological activity, or delay in closing) was neglected. Figure 4 displays the
 421 absolute pH_T differences between replicates for each cruise. The overall mean and standard deviation of these
 422 differences is 0.0014 ± 0.0015 pH_T units ($N = 502$). The highest reproducibility was obtained in 2021, with 92
 423 duplicate samples yielding a mean difference of 0.0007 ± 0.0010 pH_T units. This improved reproducibility,
 424 particularly evident during the two most recent cruises, coincides with more precise evaluations of mCP dye effects
 425 (Table 1) and likely reflects the better performance of the spectrophotometer used (PerkinElmer Lambda 800; Table
 426 1), contributing to the overall improvement in data quality. Typical reproducibility across OVIDE-BOCATS
 427 cruises ranged between 0.0007 and 0.0018 pH_T units.

428 3. Assessment of the effect of indicator dye impurities on pH_T

429 During the OVIDE-2018, BOCATS2-2021, and BOCATS2-2023 cruises, paired measurements were performed in
 430 duplicate samples collected from the same Niskin bottle and measured using two types of mCP dye: (i) purified
 431 mCP, provided by Dr. Byrne's laboratory, University of South Florida, USA (FB6 batch), and (ii) unpurified mCP,
 432 commercially available from Sigma-Aldrich (Cat. No. 211761-5G, batch #07005HH). pH_T values were obtained
 433 applying the L'11 parametrization to R values obtained with purified mCP dye, and the CB'93 parametrization
 434 combined with the DVD'98 correction (CB'93+DVD'98 hereafter) to R values obtained with unpurified mCP dye.



436 **Figure 4.** Whisker boxplots showing pH_T repeatability across OVIDE-BOCATS cruises (2002—2023),
437 represented as the absolute difference between duplicate samples collected during each cruise. The number of
438 duplicate samples analyzed per cruise were: 34 (2002), 64 (2004), 84 (2006), 21 (2008), 0 (2010), 17 (2012), 7
439 (2014), 14 (2016), 90 (2018), 92 (2021), and 79 (2023). For each cruise, the subset mean (μ) and standard deviation
440 (σ) are indicated, as well as the minimum and maximum values. The overall mean (μ_T) and standard deviation (σ_T)
441 across all 10 cruises are shown in the inset textbox. μ_T is also plotted as a horizontal dashed line, with σ_T represented
442 as a shaded gray band. Each boxplot displays the median (horizontal line), first (Q1) and third (Q3) quartiles (box
443 edges), and the minimum and maximum within 1.5 times the interquartile range (IQR = Q3 – Q1) (whiskers).

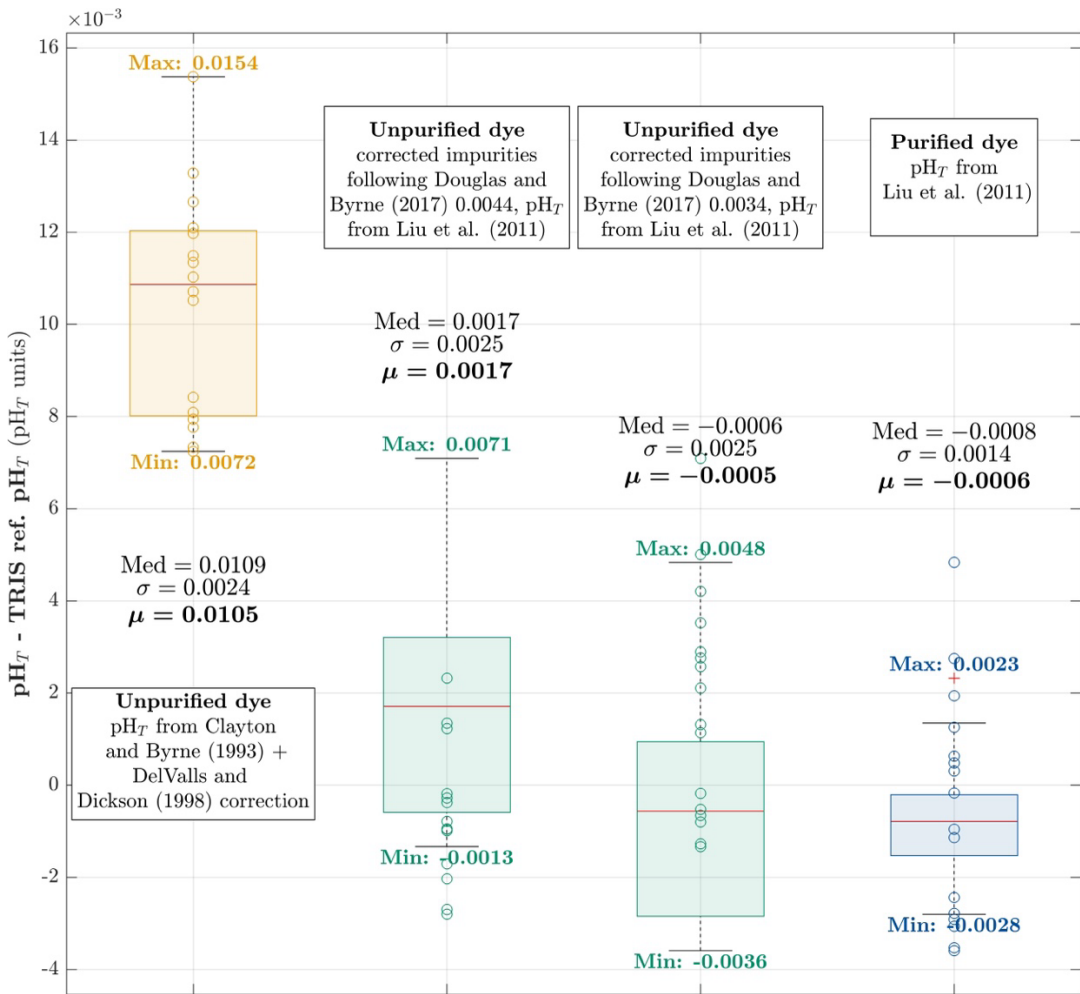
444 **3.1 TRIS buffer validation**

445 *TRIS* buffers in synthetic seawater (batch numbers 30 and 40) were obtained from Prof. Dickson's laboratory
446 (Scripps Institution of Oceanography; USA). These buffers were supplied in 125 mL borosilicate glass bottles and
447 contained an equimolar mixture of *TRIS/TRIS-HCl* in a synthetic seawater of nominal salinity 35. The reference
448 pH_T values of these batches can be calculated following DVD'98. Multiple bottles from both batches were
449 measured during the BOCATS2-2021 and BOCATS2-2023 cruises using two mCP dye solutions: (i) unpurified
450 mCP (75 μL of 2 mM solution; Sigma-Aldrich; 5.36 μM final mCP dye concentration in the sample cell), and (ii)
451 purified mCP (10 μL of 11 mM solution; provided by Prof. R. Byrne's laboratory; 3.93 μM final mCP dye
452 concentration in the sample cell).

453 Each buffer sample was measured in quadruplicate. Following blank measurement, the sample was placed in the
454 spectrophotometer's thermostated cell holder and allowed to equilibrate for 10—15 minutes. Measurements were
455 then conducted at 3-minute intervals. To ensure full thermal stabilization, only the last two measurements out of
456 the four were retained for analysis. Temperature at the end of the fourth measurement was recorded using a
457 calibrated Physics 100-1 thermometer, with an uncertainty of $\pm 0.01^\circ\text{C}$.

458 A total of 16 measurements performed using Sigma-Aldrich unpurified mCP dye, following the OVIDE-BOCATS
459 protocol (CB'93+DVD'98; see Sect. 2.2.2), showed a consistent positive bias of **0.0105 ± 0.0013 pH_T units** relative
460 to the nominal *TRIS* pH_T values (Fig. 5). In contrast, 15 measurements conducted with the purified mCP dye,
461 applying the L'11 parameterization, yielded values that were tightly centered around the nominal *TRIS* pH_T values,
462 with a negligible bias of **-0.0003 ± 0.0011 pH_T units**. No ΔR or ΔpH_T corrections were applied to either dataset, as
463 the buffer capacity of *TRIS* is approximately 20 times higher than that of seawater, rendering the impact of the mCP
464 dye addition on pH_T negligible.
465

466 The correction of ${}_{434}\text{A}_{\text{imp}}$ due to mCP dye impurities, as proposed by DB'17, was evaluated using a value of ${}_{434}\text{A}_{\text{imp}} = 0.004413$ absorbance units (given in their Table 2 for Sigma-Aldrich lot #11517KC at a mCP dye concentration
467 of 3.3 μM in the seawater sample). Applying this correction enabled the use of the L'11 parameterization,
468 substantially reducing the observed difference with purified mCP dye measurements to **0.0020 ± 0.0013 pH_T units**.
469 Recognizing that impurities can vary between batches of the same mCP dye brand, a second test using ${}_{434}\text{A}_{\text{imp}} = 0.0034$ absorbance units, consistent with that obtained by Álvarez et al. (2025), further reduced the offset to **-0.0005 ± 0.0013 pH_T units**.
470
471
472



473

474 **Figure 5.** Whisker boxplots of pH_T differences relative to TRIS buffer reference values, comparing results obtained
 475 using purified and unpurified mCP dyes. Each boxplot represents a different calculation approach: the orange
 476 boxplot shows pH_T computed using unpurified mCP dye with the CB'93 parameterization and DVD'98 correction
 477 ($N = 16$); the blue boxplot shows pH_T computed using purified mCP dye with the L'11 parameterization ($N = 15$);
 478 and green boxplots show pH_T computed using unpurified mCP dye corrected for impurities using the DB'17
 479 methodology with $_{434}\text{A}_{\text{imp}} = 0.0044$ and $_{434}\text{A}_{\text{imp}} = 0.0034$ absorbance units, respectively, and pH_T then calculated
 480 using the L'11 parameterization. Within each boxplot, the red line indicates the median (*Med*), the box edges denote
 481 the first and third quartiles, and whiskers extend to data points within 1.5 times the interquartile range. Mean (μ)
 482 and standard deviation (σ) values are provided for each subset, and the minimum and maximum values are
 483 indicated.

484 **3.2 Duplicate measurements of natural seawater**

485 During the 2021 cruise, six duplicate pH_T samples were collected at each hydrographic station along the OVIDE-
 486 BOCATS transect, with sampling points carefully distributed throughout the water column to represent different
 487 water masses. In addition to the routine pH_T determinations conducted according to the OVIDE-BOCATS protocol

488 (i.e., addition of 75 μ L of Sigma-Aldrich [2 mM] mCP dye solution and pH_T computed using CB'93+DVD'98; see
489 Sect. 2.2.2), these six replicate samples per profile were also measured using purified mCP dye (10 μ L of [11 mM]
490 mCP dye supplied by Dr. Byrne's laboratory, and pH_T determined using the L'11 parameterization).

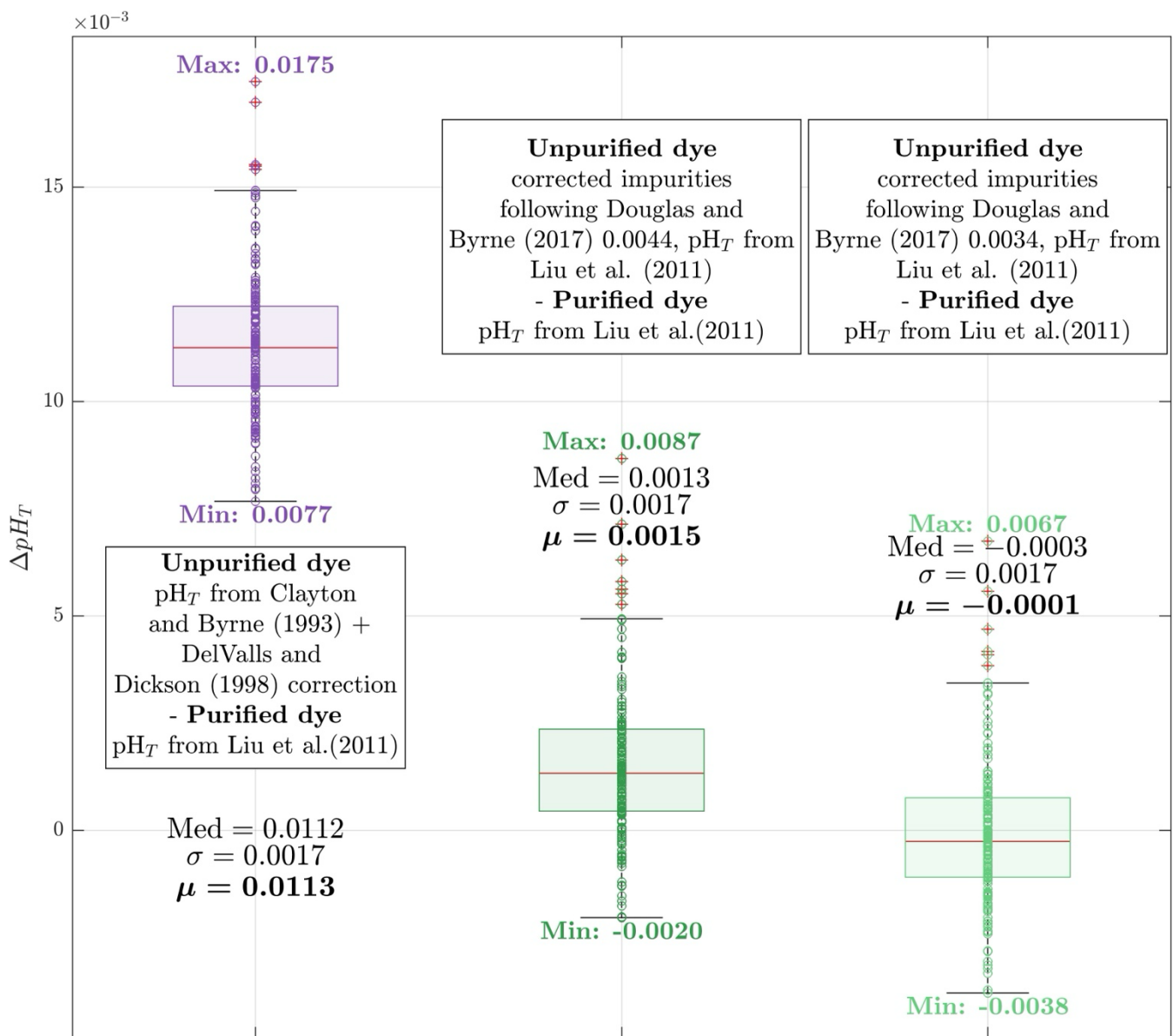
491 These duplicate measurements encompassed the full pH_T range typically observed during OVIDE-BOCATS
492 cruises (7.7 to 8.0 pH_T units). As shown in Fig. 6, the standard OVIDE-BOCATS procedure yields pH_T values that
493 are, on average, **0.0113 \pm 0.0017** ($N = 176$) pH_T units higher than those obtained using the purified mCP dye and
494 the L'11 parameterization. These results align with the findings from the *TRIS* buffer experiments (see Sect. 3.1).
495 The differences between the two methods showed no significant dependence on pH_T (Fig. 7, green dots), in
496 agreement with the theoretical expectation illustrated in Fig. 2 (blue line, Aldrich-3.4).

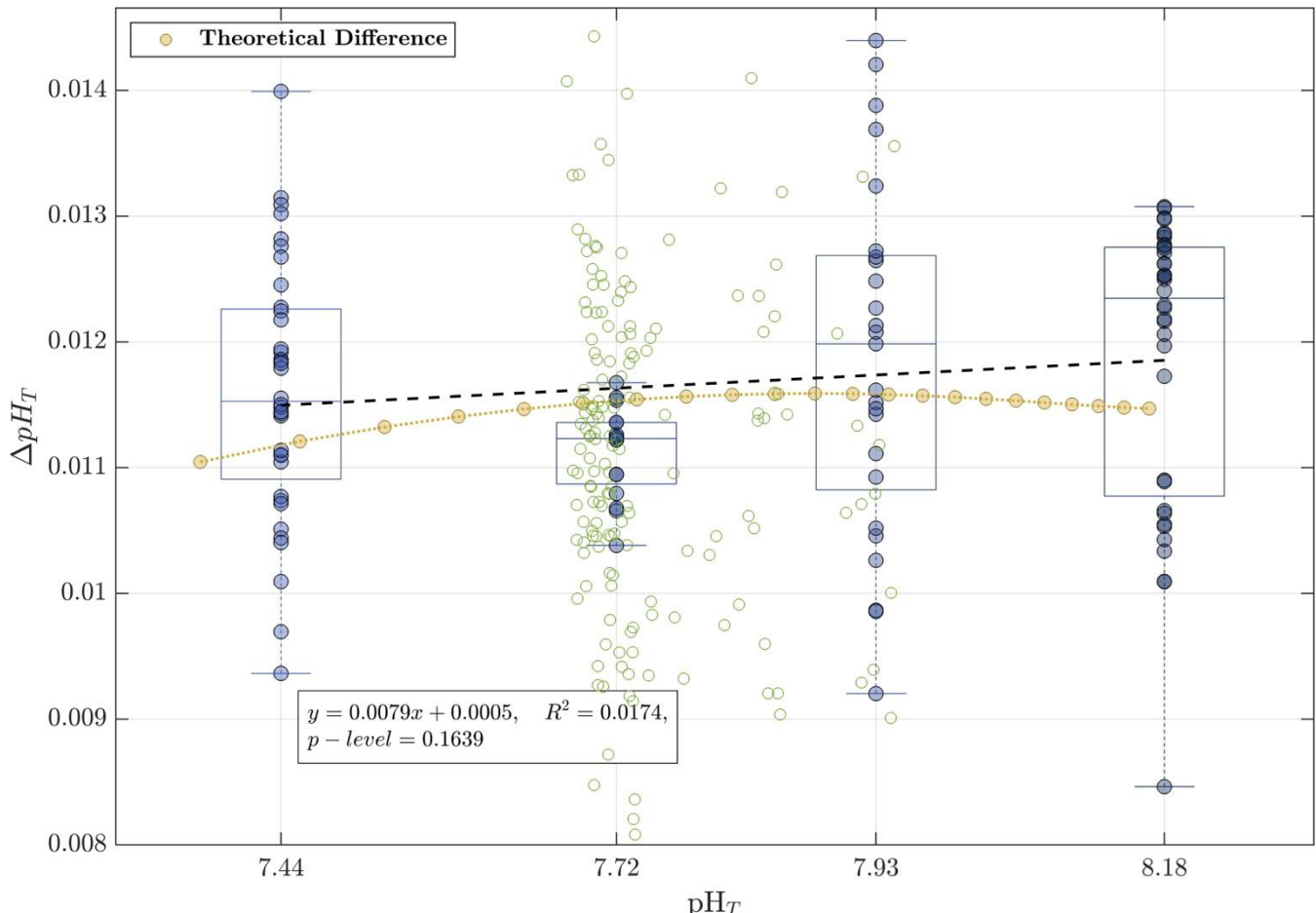
497 When the DB'17 methodology was applied using a $_{434}\text{A}_{\text{imp}}$ value of 0.004413 absorbance units at $_{488}\text{A} = 0.225$, the
498 offset was reduced to 0.0015 ± 0.0017 pH_T units—statistically indistinguishable from zero. Using a $_{434}\text{A}_{\text{imp}}$ value
499 of 0.0034 absorbance units further minimized the offset to **-0.0001 \pm 0.0017** pH_T units, corroborating the impurity
500 correction results from the *TRIS* buffer experiment. The individual $_{434}\text{A}_{\text{imp}}$ values applied here are proportionally
501 dependent on the $_{488}\text{A}$ in each measurement.

504 3.3 Duplicate measurements of modified seawater

505 During the OVIDE-2018 cruise, surface seawater with a salinity of 35.7 was treated using HCl or Na_2CO_3 to
506 produce four distinct pH_T levels (7.45, 7.70, 7.95, and 8.19). These were stored in separate Niskin bottles and
507 sampled using the same protocol as for natural seawater. For each batch, four to six samples were analyzed for pH_T
508 using the standard OVIDE-BOCATS procedure (CB'93+DVD'98 and 75 μ L of unpurified Sigma-Aldrich mCP
509 dye [2 mM] solution added to the cell; 5.36 μM final mCP dye concentration in the sample cell), and an equivalent
510 number was measured using purified mCP dye (75 μ L of mCP dye [2.5 mM] solution added to the cell; 6.70 μM
511 final mCP dye concentration in the sample cell; FB5-2017 from Dr. Byrne's laboratory and the L'11
512 parameterization). This experiment extends the comparison conducted with *TRIS* buffer and natural seawater to a
513 wider pH_T range, representative of conditions encountered in the South Atlantic and Pacific Oceans.

514 The mean pH_T offset between the two methods (measuring with unpurified mCP dye and applying CB'93+DVD'98
515 versus purified mCP dye and applying the L'11 parameterization) across 22 measurements was **0.0109 \pm 0.0011**
516 pH_T units, consistent with previous results from *TRIS* and natural seawater duplicate samples (Sect. 3.1 and Sect.
517 3.2). No significant trend was observed across the pH_T range (Fig. 7, regression p-level > 0.05). Similarly,
518 differences observed in natural seawater (green dots in Fig. 7) also showed no significant correlation with pH_T
519 (slope = -0.000 ± 0.002 ; p-level > 0.05). Furthermore, the magnitude and behavior of the observed differences are
520 consistent with theoretical expectations (Fig. 2, yellow line), assuming a $_{434}\text{A}_{\text{imp}}$ value of 0.0034 absorbance units
521 for Sigma-Aldrich mCP dye at a final concentration in the cell of 3.3 μM (as per Table 2 of DB'17).





532
 533 **Figure 7.** Differences in pH_T measurements between replicate samples measured using unpurified mCP dye
 534 (CB'93+DVD'98) and purified mCP dye (L'11 parameterization) across four pH_T levels obtained from modified
 535 seawater experiments. The black dashed line shows the linear regression of the differences as a function of pH_T ,
 536 with regression statistics summarized in the inset box. The yellow line represents the expected pH_T differences
 537 assuming a $_{434}\text{A}_{\text{imp}}$ value of 0.034 absorbance units, as modeled in Fig. 2. Green dots correspond to the 176
 538 individual pH_T differences presented in the first (purple) boxplot of Fig. 6.

539 **3.4 pH_T correction**

540 DB'17 proposed a value of $_{434}\text{A}_{\text{imp}} = 0.004413$ absorbance units for a Sigma-Aldrich mCP dye at a final
 541 concentration of $3.3 \mu\text{M}$ in the sample cell ($_{488}\text{A} = 0.225$; Takeshita et al., 2021). Based on our experimental results,
 542 we found that a better fit under our conditions corresponded to a $_{434}\text{A}_{\text{imp}}$ value of 0.0034 absorbance units, which
 543 is reasonable given that we are working with a different lot of mCP dye. Given that $_{434}\text{A}_{\text{imp}}$ is proportional to $_{488}\text{A}$,
 544 which in turn reflects the final mCP dye concentration in the cell, we derived the following relationship:

$$545 \quad _{434}\text{A}_{\text{imp}} = 0.0034 / 0.2250 \cdot _{488}\text{A} = 0.0151 \cdot _{488}\text{A} \quad (8).$$

546 Accordingly, the impurity correction was applied to each sample by subtracting the computed $_{434}\text{A}_{\text{imp}}$ (Eq. 8) from
 547 the sample measured $_{434}\text{A}$, yielding:

548 $434A_{corr,pur} = 434A - 434A_{imp} = 434A - (0.0151 \cdot 488A)$ (9),

549 $R_{corr,pur} = (578A - 730A) / (434A_{corr,pur} - 730A)$ (10),

550 where $434A_{corr,pur}$ is the corrected $434A$, and $R_{corr,pur}$ corresponds to the R value as if measured with a purified mCP
551 dye. Subsequently, pH_T was recalculated using the L'11 parameterization.

552 Implementing this correction required a comprehensive recovery and reassessment of historical $434A$, $578A$, and $488A$
553 values dating back to the 2002 cruise. Note that for data prior to 2018, $488A$ values were estimated from Eq. (7).
554 While corrections related to the mCP dye addition effect were included in the data published in GLODAPv2.2023
555 (Lauvset et al., 2024), the $488A$ -based correction described in Sect. 2.2.3 had not yet been incorporated. Final pH_T
556 values included in this work were computed from the corrected absorbance data, using the recalculated $R_{corr,pur}$,
557 along with the updated mCP dye perturbation correction $\Delta(pH_T/488A)$ -vs- $pH_{T,1}$.

561 4. Results and Discussion

562 4.1 Database product

563 We present a new database comprising 23,843 seawater samples with spectrophotometric pH_T values, each
564 accompanied by complete spatiotemporal metadata—including latitude, longitude, pressure, depth, date, and time—
565 as well as in situ measurements of temperature, salinity, and dissolved oxygen. Dissolved oxygen concentrations
566 were primarily determined using the Winkler titration method; where unavailable or deemed unreliable, values
567 from a calibrated oxygen sensor mounted on the *Conductivity, Temperature, and Depth* (CTD) instrument were
568 used. The dataset incorporates a quality flagging scheme consistent with GLODAPv2 recommendations (Key et
569 al., 2015; Olsen et al., 2016), where flag 2 denotes good data (23,773 samples), 3 (19 samples) and 4 (51 samples)
570 indicate questionable and bad data, respectively, and 9 denotes not measured.

571 Spectrophotometric pH_T data collected between 2002 and 2018, available in the GLODAPv2.2023 release (Lauvset
572 et al., 2024), were computed using the CB'93 parameterization with the DVD'98 correction (+0.0047 pH_T units).
573 The newly compiled pH_T dataset presented here updates and corrects these data following the procedure presented
574 in Sect. 3.4, applying the DB'17 adjustment and L'11 equation. In addition, the dataset significantly extends the
575 temporal coverage by including pH_T measurements from the 2021 and 2023 cruises, which were not previously
576 available; these measurements are also corrected using the same procedure, resulting in a consistent final product
577 across all cruises. In addition, for the first time, associated absorbance readings ($434A$, $578A$, and $488A$) are provided
578 alongside pH_T values. This comprehensive and corrected pH_T dataset provides a robust foundation for future
579 reassessments, such as the application of updated absorbance-to- pH_T parameterizations or transformations to
580 alternative pH scales (e.g., the "free" hydrogen ion scale).

582 4.2 Consistency of the pH_T correction

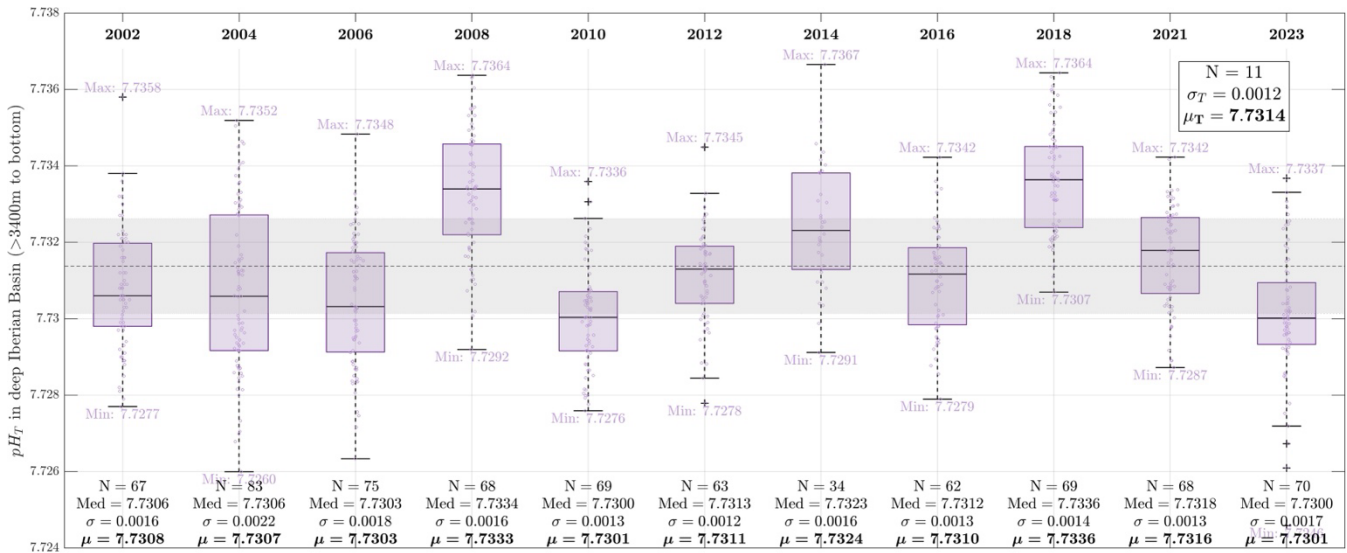
583 The differences between the former-procedure—applying the CB'93 parameterization with the DVD'98 correction
584 to R values derived from unpurified mCP dye—and the updated method presented here—applying the L'11
585 parameterization to R values derived from unpurified mCP dye corrected for the impurity effect (see Sect. 3.4)—
586 are, on average, $+0.011 \pm 0.002$ (1σ) pH_T units ($N = 23,843$; Fig. S4 in the Supplement), in line with results from
587 the assessment experiments described in Section 3. These differences show a slight negative correlation with pH_T ,
588 with smaller offsets observed at higher pH_T values (Fig. S4 in the Supplement). The slopes of the linear regressions
589 of these differences versus pH_T range from -0.0064 ± 0.0001 to 0.0005 ± 0.0001 pH_T units. It should be noted that

590 this range is comparable in magnitude to other uncertainty sources—such as the effect of the addition of mCP dye
 591 to the sample pH_T , and the instrumental measurement uncertainty (e.g., Sect. 2.2.3)—which may contribute to the
 592 overall variability in the observed differences.

593 To assess the internal consistency and long-term comparability of the corrected pH_T values, we examined the deep
 594 layer of the Iberian Basin, associated with the North East Atlantic Deep Water (NEADW). This layer has been
 595 recognized as a stable reference for the OVIDE-BOCATS program, as its properties show minimal long-term
 596 variability (García-Ibáñez et al., 2016). Supporting this minimal variability, Steinfeldt et al. (2024) reported no
 597 detectable accumulation of anthropogenic CO_2 in this layer based on chlorofluorocarbons measurements.

598 The average pH_T in the NEADW layer over 11 cruises (2002–2023) was 7.7314 ± 0.0015 (1 standard deviation;
 599 1σ), with only two cruises (2008 and 2018) exceeding the mean by more than 1 standard deviation (Fig. 8). The
 600 standard deviation within individual cruises was generally low (< 0.0018 pH_T units), with the exception of the 2004
 601 cruise (0.0022 pH_T units). Additionally, the cruise-specific mean pH_T values showed no correlation with the
 602 difference between the old and new pH_T values (Fig. S5 in the Supplement). These findings reinforce the reliability
 603 of the applied correction for the effects of impurities in the Sigma-Aldrich mCP dye (Sect. 3.4), based on a $^{434}A_{imp}$
 604 value of 0.0034 ± 0.0010 absorbance units for $_{488}A = 0.225$.

605 However, it is important to acknowledge a limitation: the $^{434}A_{imp}$ value was not directly determined for each
 606 individual batch of mCP dye, as recommended by DB'17. In practice, this is challenging—especially for older
 607 cruises—since the specific mCP dye batches may no longer be available. While Sigma-Aldrich mCP dye batches
 608 have been shown to have a narrow impurity range (typically > 90% purity; Álvarez et al., 2025), variations between
 609 batches still exist. Thus, assuming a single correction value ($^{434}A_{imp} = 0.0034$) across all cruises could be questioned.
 610 We conservatively estimate an absorbance uncertainty of ± 0.001 due to batch variability, which translates to an
 611 uncertainty of approximately ± 0.002 pH_T units. The estimate is consistent with the inter-cruise variability observed
 612 (Fig. 8), supporting the use of $^{434}A_{imp} = 0.0034$ as a reasonable and robust correction value for the entire OVIDE-
 613 BOCATS dataset.



614
 615 **Figure 8.** Variability of pH_T in the lower NEADW (deep Iberian Basin, observations > 3,400 m and east of
 616 15.45°W) during the 11 OVIDE-BOCATS cruises. These data are used to assess the internal consistency of pH_T

617 measurements over time. N refers to the number of samples analyzed in each cruise; Med indicates the median pH_T
618 of each subset (shown as a black line within each boxplot); σ is the standard deviation; and μ is the mean. Minimum
619 and maximum values are also shown for each cruise. The overall mean (μ_T ; dashed horizontal line) and standard
620 deviation (σ_T ; shaded gray band) across all 11 cruises are provided in the upper-right inset.

621 4.3 Implications of the pH_T correction on OA and aragonite saturation horizon

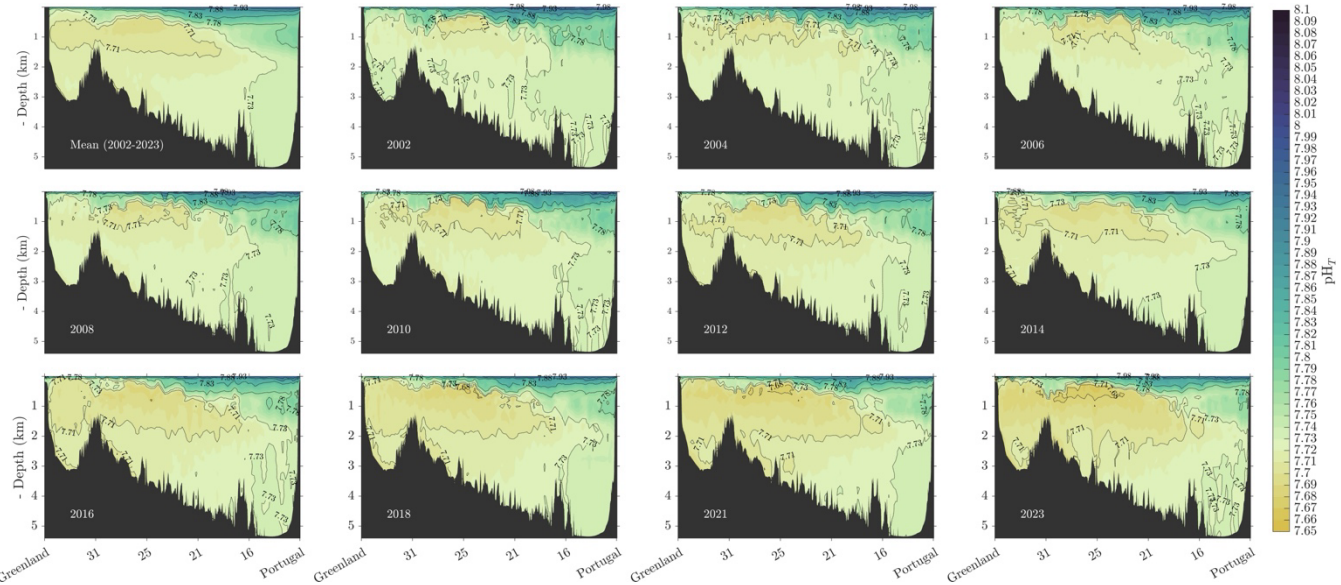
622 The correction applied to our pH_T dataset—an approximately constant offset across cruises—has negligible
623 implications for previously reported OA rates by García-Ibáñez et al. (2016) and Fontela et al. (2020a). However,
624 it does affect the calculation of the aragonite saturation, particularly the saturation horizon depth estimated by Pérez
625 et al. (2018) and García-Ibáñez et al. (2021). To assess this impact, aragonite saturation horizons were recalculated
626 using in situ temperature, salinity, A_T , and pH_T values, both before and after correcting for $_{434}A_{imp}$ (see Sect. 3.4),
627 using the carbonate chemistry constants from Lueker et al. (2000) and the boron formulation of Lee et al. (2010).
628

629 This reevaluation reveals a more pronounced reduction in aragonite saturation at the surface (from -0.040 to -
630 0.065), relative to pre-industrial conditions, which progressively diminishes with depth, reaching changes of -0.016
631 near the seafloor. Although changes at depth appear small in absolute terms, the weak vertical gradient in aragonite
632 saturation in deeper layers translates into a significant vertical shift in the saturation horizon—rising by
633 approximately 120 m to 200 m. Based on the reproducibility of the doublons (Sect. 2.2.5) and the standard
634 deviation of the mean pH_T in the NEADW layer over 11 cruises (Sect. 4.2), the uncertainty in the saturation-depth
635 change is estimated at 17 meters, while the uncertainty in the aragonite saturation state is 0.0033 units. For instance,
636 in the NA subpolar gyre, where the aragonite saturation horizon currently resides near 2,700 m depth, the revised
637 (lower) pH_T values shift it upward by approximately 150 m. This shift implies that vulnerable cold-water coral
638 ecosystems may be exposed to undersaturation conditions in shallower and more extensive regions than previously
639 estimated. This reassessment underscores the importance of accurate pH_T determinations: even subtle biases can
640 propagate into substantial differences in projected impacts on sensitive deep-sea habitats.
641

642 To investigate the spatial and temporal evolution of pH_T along the OVIDE-BOCATS section, observations from
643 the new OVIDE-BOCATS database were interpolated onto a common 7 km x 1 dbar grid. Each cruise's station
644 positions were projected onto the grid by identifying the closest grid node (minimum distance), followed by linear
645 interpolations using a Delaunay Triangulation approach (Amidror, 2002). This method ensured optimal station
646 overlap while preserving dataset consistency across years.
647

648 Figure 9 displays the pH_T distributions from the 11 cruises (2002–2023), along with the overall mean distribution.
649 Surface waters show the highest pH_T values, particularly along the eastern boundary, where elevated temperatures
650 (not shown) partly contribute to the increase. Minimum pH_T values generally occur in intermediate waters (~500–
651 1,500 m), except in the Iberian Basin, where the presence of Mediterranean Water—characterized by a warm, saline
652 core at ~1,000 m—causes a downward shift of the pH_T minimum to ~2,000 m.
653

654 Notably, a persistent pH_T minimum appears in the Iceland Basin between 500 m and 1,000 m, associated with
655 intermediate waters with high Apparent Oxygen Utilization (AOU; Fig. S6a in the Supplement; Lauvset et al.,
656 2020). This layer, influenced by older water masses transported by the North Atlantic Current (NAC) and exhibiting
657 elevated remineralization rates (de la Paz et al., 2017), has shown significant spatial expansion over time. Since
658 2016, waters with pH_T below 7.71 have progressively expanded eastward, deepening toward ~2,000 m and reaching
659 the Azores-Biscay Ridge (see Fig. 1 for georeference). In addition, the low- pH_T layer has spread into the Irminger
660 Basin since 2010.

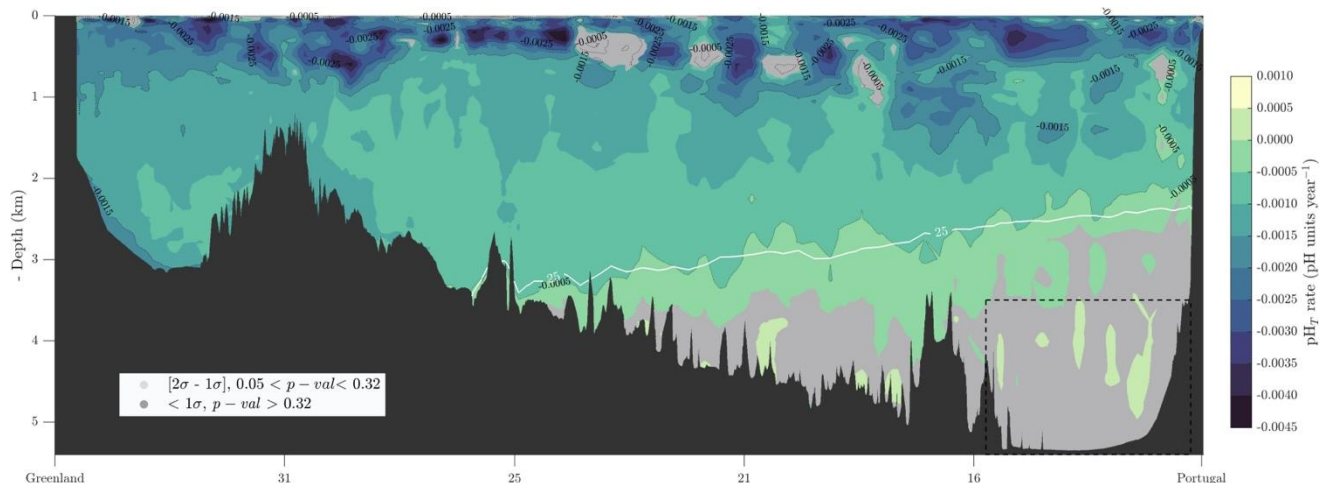


661
662 **Figure 9.** Distribution of pH_T normalized to 25°C and 1 atm along the OVIDE-BOCATS section (Fig. 1) for each
663 cruise from 2002 to 2023, as well as the overall mean of all 11 OVIDE-BOCATS cruises. The section is plotted
664 with longitudes ($^\circ\text{W}$) in the x-axis.

665
666 In the Irminger Basin, a subsurface pH_T minimum (< 7.73) was already evident in 2002, associated with DSOW.
667 This signal reappeared in 2014 with even lower values (< 7.70) and has progressively thickened through to the
668 most recent observations in 2023. Although less intense than the DSOW signal, ISOW in the Iceland Basin has
669 also shown a noticeable OA signal since 2016, reaching comparable pH_T values to those found in DSOW. In
670 contrast, the deep pH_T maximum observed in 2002 at depths of 2,700–3,000 m—extending eastward from 20°W —
671 had largely disappeared by 2010, becoming confined to the Iberian Basin. There, maximum pH_T values persist
672 between 3,000 and 5,250 m depth, corresponding to the core of NEADW.
673

674 This contrast in deep-ocean pH_T between the more recently ventilated waters of the Irminger and Iceland Basins
675 and the older, more stable NEADW is consistent with differential exposure to C_{ant} . Waters in the subpolar basins—
676 having had more recent contact with the atmosphere or mixed with recently ventilated layers—have absorbed more
677 C_{ant} , leading to their enhanced OA (Fig. 10) (García-Ibáñez et al., 2016).

678 DSOW exhibits a particularly strong OA (rate $< -0.0015 \text{ pH}_T \text{ yr}^{-1}$), extending along the bottom of the Irminger
679 Basin. A similar, though less intense, signal is seen in ISOW ($< -0.0010 \text{ pH}_T \text{ yr}^{-1}$). The highest OA rates (< -0.002
680 $\text{pH}_T \text{ yr}^{-1}$) are observed in the surface layers (0–500 m) due to direct air-sea CO_2 exchange, consistent with the rate
681 reported in Reverdin et al. (2018) for surface data in the NA subpolar gyre. These upper layers also exhibit high
682 interannual pH_T variability (Fig. S7 in the Supplement), which correlates negatively with AOU (Fig. S6b in the
683 Supplement). This pH_T -AOU relationship suggests a strong influence of mesoscale variability, particularly
684 associated with the NAC, which is known for its energetic and variable meandering in this region (Daniault et al.,
685 2016). As a result, OA rates in NAC-influenced areas may be either enhanced or masked by spatial variability of
686 the natural component in the pH_T variability, sometimes leading to non-significant OA rates despite ongoing C_{ant}
687 uptake.
688



690
691 **Figure 10.** Linear trends in pH_T at 25°C and 1 atm from 2002 to 2023 (i.e., OA rates) along the OVIDE-BOCATS
692 section (Fig. 1), based on high-resolution interpolations. Blue (yellow) shading indicates more (less) negative OA
693 rates. Grey areas denote trends that are not statistically significant at the 1σ level. The white contour represents the
694 silicate isoline of $25 \mu\text{mol kg}^{-1}$, and the dashed black box marks the deep Iberian Basin region used for measurement
695 quality-control (see Sect. 4.2). Longitude ($^\circ \text{W}$) is shown on the x-axis.

696
697 On the other hand, in the deep-water masses east to 30°W , there is a clear transition to non-significant OA rates at
698 depth (Fig. 10). This transition coincides with the $25 \mu\text{mol kg}^{-1}$ silicate isoline, which marks the boundary between
699 NA-origin waters and those with Antarctic influence (García-Ibáñez et al., 2015). At this silicate level, García-
700 Ibáñez et al. (2015) estimated that NEADW accounts for $\sim 30\%$ of the water mass composition, while LSW and
701 ISOW contribute the remaining 70% , with proportions varying with depth. NEADW originates from Antarctic
702 Bottom Water, which flows into the Eastern North Atlantic Basin from the Vema Fracture Zone (Mercier and
703 Morin, 1997), and is largely devoid of C_{ant} (Steinfeldt et al., 2024). Consequently, as silicate concentrations increase
704 beyond $25 \mu\text{mol kg}^{-1}$, the influence of NEADW becomes dominant, resulting in non-significant OA rates (Fig. 10),
705 and elevated AOU values (Fig. S6a in the Supplement), consistent with the advanced age and limited ventilation
706 of these waters.

707 5. Conclusions

708 We present a new, rigorously quality-controlled dataset of discrete spectrophotometric pH_T measurements from the
709 North Atlantic, spanning over two decades and including absorbance data. This dataset provides a unique resource
710 for the ocean carbon research community, enabling retrospective reassessment of pH_T values and derived variables
711 under updated methodological standards.

712 Our analysis revealed that pH_T values measured with an unpurified mCP dye from Sigma-Aldrich exhibit a
713 consistent positive bias of $+0.011 \pm 0.002$ pH_T units, on average, compared to those measured using purified mCP
714 dye, with this offset decreasing slightly at higher pH_T . While the correction applied has negligible influence on
715 previously published OA trends, it significantly affects derived variables such as the aragonite saturation horizon,
716 which is now estimated to be up to 200 m shallower in certain regions. These changes have implications for
717 assessing the vulnerability of deep-sea ecosystems to OA and underscore the need for highly accurate pH_T
718 measurements.

720
721 Our results reinforce findings from recent studies (e.g., Carter et al., 2024a; Takeshita et al., 2021, 2022) and
722 support the following recommendations:
723

- 724 1. Ideally, pH_T measurements should be carried out using well-characterized, purified mCP dyes and
725 following consensus procedures that ensure SI traceability (Capitaine et al., 2023; Carter et al., 2024a),
726 regardless of mCP dye used.
- 727 2. Although the correction applied here (${}_{434}\text{A}_{\text{imp}} = 0.0034$) yielded consistent results, we recommend the
728 determination of batch-specific ${}_{434}\text{A}_{\text{imp}}$ values (Douglas and Byrne, 2017; Álvarez et al., 2025).
- 729 3. The effect of mCP dye addition on sample pH_T is comparable in magnitude to spectrophotometer non-
730 linearity. Our findings support the estimation of this effect via $\Delta(\text{pH}_T/488\text{A})$ -vs- $\text{pH}_{T,i}$ approach proposed by
731 Takeshita et al. (2022), and are consistent with recommendations by Li et al. (2020).
- 732 4. While the mCP dye does not significantly alter the *TRIS* buffer pH_T , accurate temperature control is
733 essential. *TRIS* remains suitable for methodological validation, with spectrophotometer behavior being the
734 primary concern (Capitaine et al., 2023).

735 6. Data availability

736 The complete OVIDE-BOCATS pH_T dataset presented in this study is made available at
737 <https://doi.org/10.5281/zenodo.17789895> (Pérez et al., 2025) in multiple formats to ensure broad accessibility
738 and compatibility with different research workflows. The dataset includes 23,843 spectrophotometric pH_T
739 measurements along with associated absorbance data (${}_{434}\text{A}$, ${}_{578}\text{A}$, and ${}_{488}\text{A}$) and complete spatiotemporal metadata
740 from 11 cruises spanning 2002-2023. Data are provided as: (1) comma-separated values (CSV) format for general
741 use, (2) WHP-Exchange bottle format following WOCE Hydrographic Program Exchange format standards, (3)
742 NetCDF format with CF-compliant metadata, and (4) Apache Parquet format with both CF standard names and the
743 proposed metadata conventions of Jiang et al. (2022). This multi-format approach ensures the data can be readily
744 integrated into existing oceanographic databases and analysis workflows, adhering to FAIR (Findable, Accessible,
745 Interoperable, and Reusable) data principles. All formats include quality flags for pH_T following GLODAP
746 recommendations.

747 753 Supplementary Information

754 The supplement related to this article is available online at:
755

756 757 Author contribution

758 FFP, MLM, and AV designed the study, conceptualization, methodology, validation and formal analysis. AV, PL
759 and FFP give supervision, administration and funding. The manuscript was written by MLM and FFP and edited,
760 and also revised by MGI and discussed by all authors. The dataset, data curation and validation were done by FFP,
761 AV, MA and MLM.

762 763 Competing interests

764 Author A. Velo is a member of the editorial board of the journal.

765
766 **Acknowledgments**
767

768 We thank all of the scientists, technicians, personnel, and crew who were responsible for the collection and analysis
769 of the over 23 000 samples included in the final dataset.
770

771 **Financial support**
772

773 F.F. Pérez and X.A. Padín were supported by FICARAM+ (PID2023-148924OB-I00) project funded by
774 MICIU/AEI/10.13039/501100011033 and FEDER, UE. A. Velo was supported by the European Union under grant
775 agreement no. 101094690 (EuroGO-SHIP). M. López-Mozos was supported by the grant PRE2020-093138 funded
776 by MICIU/AEI/10.13039/501100011033 and by “ESF Investing in your future”. M. Fontela was funded by
777 PTA2022-021307-I, MCIN/AEI/10.13039/501100011033 and by FSE+. M.I. García-Ibáñez and M. Álvarez were
778 supported by the ESMARES (Marine Strategy Directive Framework) program funded by the Spanish Ministry for
779 the Ecological Transition and the Demographic Challenge. N.M. Fajar was supported the Complementary Science
780 Plans for Marine Science of ‘Ministerio de Ciencia, Innovación y Universidades’ included in the Recovery,
781 Transformation and Resilience Plan (PRTR-C17.II) funded through ‘Xunta de Galicia’ with Next Generation EU
782 and the European Maritime Fisheries and Aquaculture Fund.
783

783 This work has been supported by FICARAM+ (PID2023-148924OB-I00) project funded by MICIU/AEI
784 /10.13039/501100011033 and FEDER, UE.
785

786 This work was co-funded by the European Union under grant agreement no. 101094690 (EuroGO-SHIP) and UK
787 Research and Innovation (UKRI) under the UK government's Horizon Europe funding guarantee [grant numbers:
788 10051458, 10068242, 10068528]. Views and opinions expressed are however those of the author(s) only and do
789 not necessarily reflect those of the European Union or European Research Executive Agency. Neither the European
790 Union nor the granting authority can be held responsible for them.
791

792 **References**
793

794 Álvarez, M., Fajar, N. M., Carter, B. R., Guallart, E. F., Pérez, F. F., Woosley, R. J., and Murata, A.:
795 Global ocean spectrophotometric pH assessment: consistent inconsistencies, *Environ. Sci. Technol.*, **54**, 10977–
796 10988, <https://doi.org/10.1021/acs.est.9b06932>, 2020.
797

798 Álvarez, M., García-Ibáñez, M. I., Acerbi, R., Santiago-Domenech, R., Guallart, E. F., Fajar, N. M., and Arbilla,
799 L.: Ocean acidification at the crossroads I: Harmonizing unpurified and purified meta-cresol purple
800 spectrophotometric pH_T measurements based on absorbance data, *Limnol. Oceanogr. Methods*,
801 <https://doi.org/10.1002/lom3.70023>, 2025.
802

803 Álvarez-Salgado, X. A., Nieto-Cid, M., Álvarez, M., Pérez, F. F., Morin, P., and Mercier, H.:
804 New insights on the mineralization of dissolved organic matter in central, intermediate, and deep water masses of
805 the northeast North Atlantic, *Limnol. Oceanogr.*, **58**, 681–696, <https://doi.org/10.4319/lo.2013.58.2.0681>, 2013.
806

807 Amidror, I.: Scattered data interpolation methods for electronic imaging systems: A survey, *J. Electron. Imaging*,
808 **11**, 157–176, <https://doi.org/10.1117/1.1455013>, 2002.
809

810 Asselot, R., Carracedo, L. I., Thierry, V., Mercier, H., Bajon, R., and Pérez, F. F.: Anthropogenic carbon pathways
811 towards the North Atlantic interior revealed by Argo-O2, neural networks and back-calculations, *Nat. Commun.*,
812 **15**, 1630, <https://doi.org/10.1038/s41467-024-46074-5>, 2024.

813

814 Bajon, R., Carracedo, L. I., Mercier, H., Asselot, R., and Pérez, F. F.: Seasonal to long-term variability of natural and anthropogenic carbon concentrations and transports in the subpolar
815 North Atlantic Ocean, *EGUspHERE* [preprint], <https://doi.org/10.5194/egusphere-2025-4425>, 2025.

816

817 Bushinsky, S. M., Nachod, Z., Fassbender, A. J., Tamsitt, V., Takeshita, Y., and Williams, N.: Offset between profiling float and shipboard oxygen observations at depth imparts bias on float pH and derived
818 pCO₂, *Global Biogeochem. Cycles*, **39**, e2024GB008185, <https://doi.org/10.1029/2024GB008185>, 2025.

819

820

821 Byrne, R. H., and Breland, J. A.: High precision multiwavelength pH determinations in seawater using cresol red,
822 *Deep-Sea Res. Pt. A*, **36**, 803–810, 1989.

823

824

825 Caldeira, K., and Wickett, M. E.: Anthropogenic carbon and ocean pH, *Nature*, **425**, 365,
826 <https://doi.org/10.1038/425365a>, 2003.

827

828 Capitaine, G., Stoica, D., Wagener, T., and Fisicaro, P.: Production of a reference material for seawater pHT
829 measurements by a National Metrology Institute, *Mar. Chem.*, **252**, 104244,
830 <https://doi.org/10.1016/j.marchem.2023.104244>, 2023.

831

832 Carter, B. R., Feely, R. A., Williams, N. L., Dickson, A. G., Fong, M. B., and Takeshita, Y.: Updated methods for global locally interpolated estimation of alkalinity, pH, and nitrate, *Limnol. Oceanogr. Methods*, **16**, 119–131, <https://doi.org/10.1002/lom3.10232>, 2018.

833

834

835 Carter, B. R., Radich, J. A., Doyle, H. L., and Dickson, A. G.: An automated system for spectrophotometric
836 seawater pH measurements, *Limnol. Oceanogr. Methods*, **11**, 16–27, <https://doi.org/10.4319/lom.2013.11.16>,
837 2013.

838

839

840 Carter, B. R., Sharp, J. D., Dickson, A. G., Alvarez, M., Fong, M. B., García-Ibáñez, M. I., and Wang, Z. A.: Uncertainty sources for measurable ocean carbonate chemistry variables, *Limnol. Oceanogr.*, **69**, 1–21,
841 <https://doi.org/10.1002/lno.12477>, 2024a.

842

843

844 Carter, B. R., Sharp, J. D., García-Ibáñez, M. I., Woosley, R. J., Fong, M. B., Alvarez, M., and Wang, Z. A.: Random and systematic uncertainty in ship-based seawater carbonate chemistry observations, *Limnol. Oceanogr.*,
845 **69**, 2473–2488, <https://doi.org/10.1002/lno.12674>, 2024b.

846

847

848 Chierici, M., Fransson, A., and Anderson, L. G.: Influence of m-cresol purple indicator additions on the pH of
849 seawater samples: Correction factors evaluated from a chemical speciation model, *Mar. Chem.*, **65**, 281–290,
850 [https://doi.org/10.1016/S0304-4203\(99\)00020-1](https://doi.org/10.1016/S0304-4203(99)00020-1), 1999.

851

852 Clayton, T. D., and Byrne, R. H.: Spectrophotometric seawater pH measurements: Total hydrogen ion
853 concentration scale calibration of m-cresol purple and at-sea results, *Deep-Sea Res. Pt. I*, **40**, 2115–2129,
854 [https://doi.org/10.1016/0967-0637\(93\)90048-8](https://doi.org/10.1016/0967-0637(93)90048-8), 1993.

855

856 Daniault, N., Mercier, H., Lherminier, P., Sarafanov, A., Falina, A., Zunino, P., Pérez, F. F., Ríos, A. F., Ferron,
857 B., Huck, T., Thierry, V., and Gladyshev, S.: The northern North Atlantic Ocean mean circulation in the early
858 21st century, *Prog. Oceanogr.*, **146**, 142–158, <https://doi.org/10.1016/j.pocean.2016.06.007>, 2016.

859 de la Paz, M., García-Ibáñez, M. I., Steinfeldt, R., Ríos, A. F., and Pérez, F. F.: Ventilation versus biology: What
860 is the controlling mechanism of nitrous oxide distribution in the North Atlantic?, *Global Biogeochem. Cycles*, **31**,
861 745–760, <https://doi.org/10.1002/2016GB005507>, 2017.

862 DelValls, T., and Dickson, A.: The pH of buffers based on 2-amino-2-hydroxymethyl-1,3-propanediol (tris) in
863 synthetic seawater, *Deep-Sea Res. Pt. I*, **45**, 1541–1554, [https://doi.org/10.1016/S0967-0637\(98\)00019-3](https://doi.org/10.1016/S0967-0637(98)00019-3), 1998.

864 DeVries, T., Yamamoto, K., Wanninkhof, R., Gruber, N., Hauck, J., Müller, J. D., Bopp, L., Carroll, D., Carter,
865 B., Chau, T.-T.-T., Doney, S. C., Gehlen, M., Gloege, L., Gregor, L., Henson, S., Kim, J. H., Iida, Y., Ilyina, T.,
866 Landschützer, P., Le Quéré, C., Munro, D., Nissen, C., Patara, L., Pérez, F. F., Resplandy, L., Rodgers, K. B.,
867 Schwinger, J., Séférian, R., Sicardi, V., Terhaar, J., Triñanes, J., Tsujino, H., Watson, A., Yasunaka, S., and Zeng,
868 J.: Magnitude, trends, and variability of the global ocean carbon sink from 1985 to 2018, *Global Biogeochem.*
869 *Cycles*, **37**, e2023GB007780, <https://doi.org/10.1029/2023GB007780>, 2023.

870

871 Dickson, A. G.: The measurement of sea water pH, *Mar. Chem.*, **44**, 131–142, [https://doi.org/10.1016/0304-4203\(93\)90198-W](https://doi.org/10.1016/0304-4203(93)90198-W), 1993.

872

873

874 Dickson, A. G.: Standards for ocean measurements, *Oceanography*, **23**, 34–47,
875 <https://www.jstor.org/stable/24860884>, 2010.

876

877 Dickson, A. G., Sabine, C. L., and Christian, J. R. (Eds.): *Guide to best practices for ocean CO₂ measurements*,
878 PICES Special Publication 3, <https://www.oceandatapractices.org/handle/11329/249>, 2007.

879

880 Douglas, N. K., and Byrne, R. H.: Achieving accurate spectrophotometric pH measurements using unpurified meta-
881 cresol purple, *Mar. Chem.*, **190**, 66–72, <https://doi.org/10.1016/j.marchem.2017.02.004>, 2017.

882

883 Fong, M. B., Takeshita, Y., Easley, R. A., and Waters, J. F.:
884 Detection of impurities in m-cresol purple with Soft Independent Modeling of Class Analogy for the quality control
885 of spectrophotometric pH measurements in seawater, *Mar. Chem.*, **259**, 104362,
886 <https://doi.org/10.1016/j.marchem.2024.104362>, 2024.

887

888 Fontela, M., Mercier, H., and Pérez, F. F.: Long-term integrated biogeochemical budget driven by circulation in
889 the eastern subpolar North Atlantic, *Prog. Oceanogr.*, **173**, 51–65, <https://doi.org/10.1016/j.pocean.2019.02.004>,
890 2019.

891

892 Fontela, M., Pérez, F. F., Carracedo, L. I., Padín, X. A., Velo, A., García-Ibáñez, M. I., and Lherminier, P.: The
893 Northeast Atlantic is running out of excess carbonate in the horizon of cold-water coral communities, *Sci. Rep.*, **10**,
894 71793, <https://doi.org/10.1038/s41598-020-71793-2>, 2020a.

895

896 Fontela, M., Pérez, F. F., Mercier, H., and Lherminier, P.: North Atlantic western boundary currents are intense
897 dissolved organic carbon streams, *Front. Mar. Sci.*, **7**, 593757, <https://doi.org/10.3389/fmars.2020.593757>, 2020b.

898

899 Fontela, M., Velo, A., Brown, P. J., and Pérez, F. F.:
 900 Carbonate system species and pH, in: *Marine Analytical Chemistry*, Blasco, J. and Tovar-Sánchez, A. (Eds.),
 901 Springer, Cham, https://doi.org/10.1007/978-3-031-14486-8_1, 2023.

902

903 Friedlingstein, P., O'Sullivan, M., Jones, M. W., Andrew, R. M., Bakker, D. C. E., Hauck, J., Landschützer, P., Le
 904 Quéré, C., Luijkx, I. T., Peters, G. P., Peters, W., Pongratz, J., Schwingshackl, C., Sitch, S., Canadell, J. G., Ciais,
 905 P., Jackson, R. B., Alin, S. R., Anthoni, P., and Zheng, B.:
 906 Global Carbon Budget 2023, *Earth Syst. Sci. Data*, **15**, 5301–5369, <https://doi.org/10.5194/essd-15-5301-2023>,
 907 2023.

908

909 García-Ibáñez, M. I., Bates, N. R., Bakker, D. C. E., Fontela, M., and Velo, A.:
 910 Cold-water corals in the subpolar North Atlantic Ocean exposed to aragonite undersaturation if the 2 °C global
 911 warming target is not met, *Glob. Planet. Change*, **201**, 103480, <https://doi.org/10.1016/j.gloplacha.2021.103480>,
 912 2021.

913

914 García-Ibáñez, M. I., Pardo, P. C., Carracedo, L. I., Mercier, H., Lherminier, P., Ríos, A. F., and Pérez, F. F.:
 915 Structure, transports and transformations of the water masses in the Atlantic Subpolar Gyre, *Prog. Oceanogr.*, **135**,
 916 18–36, <https://doi.org/10.1016/j.pocean.2015.03.009>, 2015.

917

918 García-Ibáñez, M. I., Zunino, P., Fröb, F., Carracedo, L. I., Ríos, A. F., Mercier, H., Olsen, A., and Pérez, F. F.:
 919 Ocean acidification in the subpolar North Atlantic: Rates and mechanisms controlling pH changes, *Biogeosciences*,
 920 **13**, 3701–3715, <https://doi.org/10.5194/bg-13-3701-2016>, 2016.

921

922 Gattuso, J.-P., Magnan, A., Billé, R., Cheung, W. W. L., Howes, E. L., Joos, F., Allemand, D., Bopp, L., Cooley,
 923 S. R., Eakin, C. M., Hoegh-Guldberg, O., Kelly, R. P., Pörtner, H.-O., Rogers, A. D., Baxter, J. M., Laffoley, D.,
 924 Osborn, D., Rankovic, A., Rochette, J., and Turley, C.:
 925 Contrasting futures for ocean and society from different anthropogenic CO₂ emissions scenarios, *Science*, **349**,
 926 aac4722, <https://doi.org/10.1126/science.aac4722>, 2015.

927

928 Gehlen, M., Séférian, R., Jones, D. O. B., Roy, T., Roth, R., Barry, J., Bopp, L., Doney, S. C., Dunne, J. P., Heinze,
 929 C., Joos, F., Orr, J. C., Resplandy, L., Segschneider, J., and Tjiputra, J.:
 930 Projected pH reductions by 2100 might put deep North Atlantic biodiversity at risk, *Biogeosciences*, **11**, 6955–
 931 6967, <https://doi.org/10.5194/bg-11-6955-2014>, 2014.

932

933 IPCC: *IPCC Special Report on the Ocean and Cryosphere in a Changing Climate*, Intergovernmental Panel on
 934 Climate Change, 2019.

935

936 Jiang, L. Q., Pierrot, D., Wanninkhof, R., Feely, R. A., Tilbrook, B., Alin, S., Barbero, L., Byrne, R. H., Carter, B.
 937 R., Dickson, A. G., Gattuso, J. P., Greeley, D., Hoppema, M., Humphreys, M. P., Karstensen, J., Lange, N.,
 938 Lauvset, S. K., Lewis, E. R., Olsen, A., Pérez, F. F., Sabine, C., Sharp, J. D., Tanhua, T., Trull, T. W., Velo, A.,
 939 Allegra, A. J., Barker, P., Burger, E., Cai, W. J., Chen, C. T. A., Cross, J., Garcia, H., Hernandez-Ayon, J. M., Hu,
 940 X., Kozyr, A., Langdon, C., Lee, K., Salisbury, J., Wang, Z. A., and Xue, L.: Best practice data standards for
 941 discrete chemical oceanographic observations, *Front. Mar. Sci.*, **8**, 705638,
 942 <https://doi.org/10.3389/fmars.2021.705638>, 2022.

943

944 Key, R. M., Olsen, A., van Heuven, S., Lauvset, S. K., Velo, A., Lin, X., Schirnick, C., Kozyr, A., Tanhua, T.,
945 Hoppema, M., Jutterstrom, S., Steinfeldt, R., Jeansson, E., Ishii, M., Perez, F. F., and Suzuki, T.: Global Ocean Data Analysis Project, Version 2 (GLODAPv2), ORNL/CDIAC-162, ND-P093, Carbon Dioxide
946 Information Analysis Center (CDIAC), https://doi.org/10.3334/CDIAC/OTG.NDP093_GLODAPv2, 2015.
947

948 Kwiatkowski, L., and Orr, J. C.: Diverging seasonal extremes for ocean acidification during the twenty-first
949 century, *Nat. Clim. Change*, **8**, 141–145, <https://doi.org/10.1038/s41558-017-0054-0>, 2018.
950

951 Lauvset, S. K., Carter, B. R., Perez, F. F., Jiang, L.-Q., Feely, R. A., Velo, A., and Olsen, A.: Processes driving global interior ocean pH distribution, *Global Biogeochem. Cycles*, **34**, e2019GB006229,
952 <https://doi.org/10.1029/2019GB006229>, 2020.
953

954 Lauvset, S. K., Lange, N., Tanhua, T., Bittig, H. C., Olsen, A., Kozyr, A., Álvarez, M., Azetsu-Scott, K., Brown,
955 P. J., Carter, B. R., Cotrim da Cunha, L., Hoppema, M., Humphreys, M. P., Ishii, M., Jeansson, E., Murata, A.,
956 Müller, J. D., Pérez, F. F., Schirnick, C., Steinfeldt, R., Suzuki, T., Ulfbo, A., Velo, A., Woosley, R. J., and Key,
957 R. M.: The annual update GLODAPv2.2023: the global interior ocean biogeochemical data product, *Earth Syst.
958 Sci. Data*, **16**, 2047–2072, <https://doi.org/10.5194/essd-16-2047-2024>, 2024.
959

960

961 Le Quéré, C., Moriarty, R., Andrew, R. M., Canadell, J. G., Sitch, S., Korsbakken, J. I., Friedlingstein, P., Peters,
962 G. P., Andres, R. J., Boden, T. A., Houghton, R. A., House, J. I., Keeling, R. F., Tans, P., Arneth, A., Bakker, D.
963 C. E., Barbero, L., Bopp, L., Chang, J., and Zeng, N.: Global Carbon Budget 2015, *Earth Syst. Sci. Data*, **7**, 349–396, <https://doi.org/10.5194/essd-7-349-2015>, 2015.
964

965

966 Lee, K., Kim, T. W., Byrne, R. H., Millero, F. J., Feely, R. A., and Liu, Y. M.: The universal ratio of boron to chlorinity for the North Pacific and North Atlantic oceans, *Geochim. Cosmochim. Acta*, **74**, 1801–1811, <https://doi.org/10.1016/j.gca.2009.12.027>, 2010.
967

968

969 Lee, K., Millero, F. J., Byrne, R. H., Feely, R. A., and Wanninkhof, R.: The recommended dissociation constants for carbonic acid in seawater, *Geophys. Res. Lett.*, **27**, 229–232,
970 <https://doi.org/10.1029/1999GL002345>, 2000.
971

972

973 Lherminier, P., Mercier, H., Huck, T., Gourcuff, C., Perez, F. F., Morin, P., Sarafanov, A., and Falina, A.: The
974 Atlantic Meridional Overturning Circulation and the subpolar gyre observed at the A25-OVIDE section in June
975 2002 and 2004, *Deep-Sea Res. Pt. I*, **57**, 1374–1391, <https://doi.org/10.1016/j.dsr.2010.07.009>, 2010.
976

977

978 Li, X., García-Ibáñez, M. I., Carter, B. R., Chen, B., Li, Q., Easley, R. A., and Cai, W.-J.: Purified meta-cresol purple dye perturbation: How it influences spectrophotometric pH measurements, *Mar. Chem.*, **225**, 103849, <https://doi.org/10.1016/j.marchem.2020.103849>, 2020.
979

980

981 Liu, X., Patsavas, M. C., and Byrne, R. H.: Purification and characterization of meta-cresol purple for
982 spectrophotometric seawater pH measurements, *Environ. Sci. Technol.*, **45**, 4862–4868,
983 <https://doi.org/10.1021/es200665d>, 2011.
984

985

986 Loucaides, S., Rèrolle, V. M., Papadimitriou, S., Kennedy, H., Mowlem, M. C., Dickson, A. G., and Achterberg,
987 E. P.: Characterization of meta-cresol purple for spectrophotometric pH measurements in saline and hypersaline
988 media at sub-zero temperatures, *Sci. Rep.*, **7**, 2481, <https://doi.org/10.1038/s41598-017-02624-0>, 2017.
989

990
991 Lueker, T. J., Dickson, A. G., and Keeling, C. D.: Ocean pCO₂ calculated from dissolved inorganic carbon,
992 alkalinity, and equations for K1 and K2: Validation based on laboratory measurements of CO₂ in gas and seawater
993 at equilibrium, *Mar. Chem.*, **70**, 105–119, [https://doi.org/10.1016/S0304-4203\(00\)00022-0](https://doi.org/10.1016/S0304-4203(00)00022-0), 2000.
994
995 Ma, J., Shu, H., Yang, B., Byrne, R. H., and Yuan, D.: Spectrophotometric determination of pH and carbonate ion
996 concentrations in seawater: Choices, constraints and consequences, *Anal. Chim. Acta*, **1081**, 18–31,
997 <https://doi.org/10.1016/j.aca.2019.06.024>, 2019.
998
999 Maurer, T. L., Plant, J. N., and Johnson, K. S.: Delayed-mode quality control of oxygen, nitrate, and pH data on
1000 SOCCOM biogeochemical profiling floats, *Front. Mar. Sci.*, **8**, 683207,
1001 <https://doi.org/10.3389/fmars.2021.683207>, 2021.
1002
1003 Mercier, H., Desbruyères, D., Lherminier, P., Velo, A., Carracedo, L., Fontela, M., and Pérez, F. F.: New insights into the eastern subpolar North Atlantic meridional overturning circulation from OVIDE, *Ocean Sci.*,
1004 **20**, 779–797, <https://doi.org/10.5194/os-20-779-2024>, 2024.
1005
1006 Mercier, H., and Morin, P.: Hydrography of the Romanche and Chain Fracture Zones, *J. Geophys. Res. Oceans*,
1007 **102**, 10373–10389, <https://doi.org/10.1029/97JC00229>, 1997.
1008
1009 Müller, J. D., Bastkowski, F., Sander, B., Seitz, S., Turner, D. R., Dickson, A. G., and Rehder, G.: Metrology for pH measurements in brackish waters – Part 1: Extending electrochemical pH measurements of
1010 TRIS buffers to salinities 5–20, *Front. Mar. Sci.*, **5**, 176, <https://doi.org/10.3389/fmars.2018.00176>, 2018.
1011
1012 Olsen, A., Key, R. M., van Heuven, S., Lauvset, S. K., Velo, A., Lin, X., Schirnick, C., Kozyr, A., Tanhua, T.,
1013 Hoppema, M., Jutterström, S., Steinfeldt, R., Jeansson, E., Ishii, M., Pérez, F. F., and Suzuki, T.: The Global Ocean Data Analysis Project version 2 (GLODAPv2) – an internally consistent data product for the
1014 world ocean, *Earth Syst. Sci. Data*, **8**, 297–323, <https://doi.org/10.5194/essd-8-297-2016>, 2016.
1015
1016 Olsen, A., Lange, N., Key, R. M., Tanhua, T., Álvarez, M., Becker, S., Bittig, H. C., Carter, B. R., Cotrim da
1017 Cunha, L., Feely, R. A., van Heuven, S., Hoppema, M., Ishii, M., Jeansson, E., Jones, S. D., Jutterström, S., Karlsen,
1018 M. K., Kozyr, A., Lauvset, S. K., and Wanninkhof, R.: GLODAPv2.2019 – An update of GLODAPv2, *Earth Syst. Sci. Data*, **11**, 1437–1461, <https://doi.org/10.5194/essd-11-1437-2019>, 2019.
1019
1020 Orr, J. C., Fabry, V. J., Aumont, O., Bopp, L., Doney, S. C., Feely, R. A., Gnanadesikan, A., Gruber, N., Ishida,
1021 A., Joos, F., Key, R. M., Lindsay, K., Maier-Reimer, E., Matear, R., Monfray, P., Mouchet, A., Najjar, R. G.,
1022 Plattner, G.-K., Rodgers, K. B., and Yool, A.: Anthropogenic ocean acidification over the twenty-first century and
1023 its impact on calcifying organisms, *Nature*, **437**, 681–686, <https://doi.org/10.1038/nature04095>, 2005.
1024
1025 Pérez, F. F., Fontela, M., García-Ibáñez, M. I., Mercier, H., Velo, A., Lherminier, P., Zunino, P., Paz, M. de la,
1026 Alonso-Pérez, F., Guallart, E. F., and Padin, X. A.: Meridional overturning circulation conveys fast acidification
1027 to the deep Atlantic Ocean, *Nature*, **554**, 515–518, <https://doi.org/10.1038/nature25493>, 2018.
1028
1029 Pérez, F. F., López-Mozos, M., Fontela, M., García-Ibáñez, M. I., Fajar, N. M., Padin, X. A., Castaño-Carrera, M.,
1030 de la Paz, M., Carracedo, L. I., Álvarez, M., Lherminier, P., and Velo, A.:
1031
1032
1033
1034
1035

1036 Two decades of pHT measurements along the GO-SHIP A25 section – Dataset, *Zenodo*,
1037 <https://doi.org/10.5281/zenodo.17789895>, 2025.

1038

1039 Pérez, F. F., Mercier, H., Vázquez-Rodríguez, M., Lherminier, P., Velo, A., Pardo, P. C., Rosón, G., and Ríos, A.
1040 F.: Atlantic Ocean CO₂ uptake reduced by weakening of the meridional overturning circulation, *Nat. Geosci.*, **6**,
1041 146–152, <https://doi.org/10.1038/ngeo1680>, 2013.

1042

1043 Pérez, F. F., Olafsson, J., Ólafsdóttir, S. R., Fontela, M., and Takahashi, T.:
1044 Contrasting drivers and trends of ocean acidification in the subarctic Atlantic, *Sci. Rep.*, **11**, 93324,
1045 <https://doi.org/10.1038/s41598-021-93324-3>, 2021.

1046

1047 Pérez, F. F., Becker, M., Goris, N., Gehlen, M., López-Mozos, M., Tjiputra, J., Olsen, A., Müller, J. D., Huertas,
1048 I. E., Chau, T. T. T., Cainzos, V., Velo, A., Benard, G., Hauck, J., and Gruber, N.:
1049 An assessment of CO₂ storage and sea–air fluxes for the Atlantic Ocean and Mediterranean Sea between 1985 and
1050 2018, *Global Biogeochemical Cycles*, **37**, e2023GB007862, <https://doi.org/10.1029/2023GB007862>, 2023.

1051

1052 Ramette, R. W., Culberson, C. H., and Bates, R. G.: Acid-base properties of tris(hydroxymethyl)aminomethane
1053 (Tris) buffers in sea water from 5 to 40 °C, *Anal. Chem.*, **49**, 867–870, <https://doi.org/10.1021/ac50014a049>, 1977.

1054

1055 Resplandy, L., Bopp, L., Orr, J. C., and Dunne, J. P.: Role of mode and intermediate waters in future ocean
1056 acidification: Analysis of CMIP5 models, *Geophys. Res. Lett.*, **40**, 3091–3095, <https://doi.org/10.1002/grl.50414>,
1057 2013.

1058

1059 Reverdin, G., Metzl, N., Olafsdottir, S., Racapé, V., Takahashi, T., Benetti, M., Valdimarsson, H., Benoit-Cattin,
1060 A., Danielsen, M., Fin, J., Naamar, A., Pierrot, D., Sullivan, K., Bringas, F., and Goni, G.:
1061 SURATLANT: A 1993–2017 surface sampling in the central part of the North Atlantic subpolar gyre, *Earth Syst.
Sci. Data*, **10**, 1901–1924, <https://doi.org/10.5194/essd-10-1901-2018>, 2018.

1063

1064 Rivaro, P., Vivado, D., Falco, P., and Ianni, C.: HPLC-DAD purification and characterization of meta-cresol-purple
1065 for spectrophotometric seawater pH measurements, *Water*, **13**, 3030, <https://doi.org/10.3390/w13213030>, 2021.

1066 Robert-Baldo, G. L., Morris, M. J., and Byrne, R. H.: Spectrophotometric determination of seawater pH using
1067 phenol red, *Anal. Chem.*, **57**, 2564–2567, 1985.

1068

1069 Rodgers, K. B., Schwinger, J., Fassbender, A. J., Landschützer, P., Yamaguchi, R., Frenzel, H., Stein, K., Müller,
1070 J. D., Goris, N., Sharma, S., Bushinsky, S., Chau, T.-T.-T., Gehlen, M., Gallego, M. A., Gloege, L., Gregor, L.,
1071 Gruber, N., Hauck, J., Iida, Y., and Velo, A.: Seasonal variability of the surface ocean carbon cycle: A synthesis,
1072 *Global Biogeochem. Cycles*, **37**, e2023GB007798, <https://doi.org/10.1029/2023GB007798>, 2023.

1073

1074 Sabine, C. L., Feely, R. A., Gruber, N., Key, R. M., Lee, K., Bullister, J. L., Wanninkhof, R., Wong, C. S., Wallace,
1075 D. W. R., Tilbrook, B., Millero, F. J., Peng, T.-H., Kozyr, A., Ono, T., and Rios, A. F.: The oceanic sink for
1076 anthropogenic CO₂, *Science*, **305**, 367–371, <https://doi.org/10.1126/science.1097403>, 2004.

1077

1078 Steinfeldt, R., Rhein, M., and Kieke, D.: Anthropogenic carbon storage and its decadal changes in the Atlantic
1079 between 1990–2020, *Biogeosciences*, **21**, 3839–3867, <https://doi.org/10.5194/bg-21-3839-2024>, 2024

1080

1081 Takeshita, Y., Johnson, K. S., Coletti, L. J., Jannasch, H. W., Walz, P. M., and Warren, J. K.:

1082 Assessment of pH dependent errors in spectrophotometric pH measurements of seawater, *Mar. Chem.*, **223**,
1083 103801, <https://doi.org/10.1016/j.marchem.2020.103801>, 2020.

1084

1085 Takeshita, Y., Johnson, K. S., Martz, T. R., Plant, J. N., and Sarmiento, J. L.:
1086 Assessment of autonomous pH measurements for determining surface seawater partial pressure of CO₂, *J. Geophys.*
1087 *Res. Oceans*, **123**, 4003–4013, <https://doi.org/10.1029/2017JC013387>, 2018.

1088

1089 Takeshita, Y., Mertz, K. L., Norgaard, A., Gray, S., Verburg, M. H., and Bockmon, E. E.: Accurate
1090 spectrophotometric pH measurements made directly in the sample bottle using an aggregated dye perturbation
1091 approach, *Limnol. Oceanogr. Methods*, **20**, 281–287, <https://doi.org/10.1002/lom3.10486>, 2022.

1092

1093 Takeshita, Y., Warren, J. K., Liu, X., Spaulding, R. S., Byrne, R. H., Carter, B. R., DeGrandpre, M. D., Murata,
1094 A., and Watanabe, S.: Consistency and stability of purified meta-cresol purple for spectrophotometric pH
1095 measurements in seawater, *Mar. Chem.*, **236**, 104018, <https://doi.org/10.1016/j.marchem.2021.104018>, 2021.

1096

1097 Vázquez-Rodríguez, M., Pérez, F. F., Velo, A., Ríos, A. F., and Mercier, H.: Observed acidification trends in North
1098 Atlantic water masses, *Biogeosciences*, **9**, 5217–5230, <https://doi.org/10.5194/bg-9-5217-2012>, 2012.

1099

1100 Woosley, R. J.: Long-term stability and storage of meta-cresol purple solutions for seawater pH measurements,
1101 *Limnol. Oceanogr. Methods*, **19**, 810–817, <https://doi.org/10.1002/lom3.10462>, 2021.

1102

1103 Yao, W., Liu, X., and Byrne, R. H.: Impurities in indicators used for spectrophotometric seawater pH
1104 measurements: Assessment and remedies, *Mar. Chem.*, **107**, 167–172,
1105 <https://doi.org/10.1016/j.marchem.2007.06.012>, 2007.

1106

1107 Zunino, P., Lherminier, P., Mercier, H., Padín, X. A., Ríos, A. F., and Pérez, F. F.: Dissolved inorganic carbon
1108 budgets in the eastern subpolar North Atlantic in the 2000s from in situ data, *Geophys. Res. Lett.*, **42**, 9853–9861,
1109 <https://doi.org/10.1002/2015GL066243>, 2015.

1110